

Chapter 18

Structure Formation in Thin Liquid-Liquid Films

Sebastian Jachalski, Dirk Peschka, Stefan Bommer, Ralf Seemann,
and Barbara Wagner

Abstract We revisit the problem of a liquid polymer that dewets from another liquid polymer substrate with the focus on the direct comparison of results from mathematical modeling, rigorous analysis, numerical simulation and experimental investigations of rupture, dewetting dynamics and equilibrium patterns of a thin liquid-liquid system. The experimental system uses as a model system a thin polystyrene (PS)/polymethylmethacrylate (PMMA) bilayer of a few hundred nm. The polymer systems allow for in situ observation of the dewetting process by atomic force microscopy (AFM) and for a precise ex situ imaging of the liquid-liquid interface. In the present study, the molecular chain length of the used polymers is chosen such that the polymers can be considered as Newtonian liquids. However, by increasing the chain length, the rheological properties of the polymers can be also tuned to a viscoelastic flow behavior. The experimental results are compared with the predictions based on the thin film models. The system parameters like contact angle and surface tensions are determined from the experiments and used for a quantitative comparison. We obtain excellent agreement for transient drop shapes on their way towards equilibrium, as well as dewetting rim profiles and dewetting dynamics.

18.1 Introduction

Even though liquid-liquid dewetting has been investigated to a certain extent in the past, there is still a lack of the underpinning understanding of the precise morphology and dynamics of the interfaces involved in such systems. A fundamental understanding is however crucial for many important nanofluidic problems in

S. Jachalski • D. Peschka • B. Wagner (✉)
Weierstraß Institute, Mohrenstr. 39, 10117 Berlin, Germany
e-mail: sebastian.jachalski@wias-berlin.de; dirk.peschka@wias-berlin.de;
barbara.wagner@wias-berlin.de

S. Bommer • R. Seemann
Experimental Physics, Saarland University, 66123 Saarbrücken, Germany
e-mail: stefan.bommer@physik.uni-saarland.de; r.seemann@physik.uni-saarland.de

nature and technology ranging from rupture of the human tear film to the interface dynamics of donor/acceptor polymer solutions used in organic solar cells.

Indeed, in contrast to the large body of literature in the field of liquid-solid dewetting, theoretical investigations, after the early fundamental works of Brochard-Wyart et al. [1], are rather limited. Notable exceptions are in particular the works by Pototsky et al. [2, 3], the work by Fisher and Golovin [4, 5] and by Bandyopadhyay et al. [6] and Bandyopadhyay and Sharma [7]. Linear stability analysis and numerical simulations of the short- and long-time evolution have been performed by Pototsky et al. [3], Fisher and Golovin [4], and by Bandyopadhyay et al. [6], even in the presence of surfactants [5]. However, the mathematical theory of the fully non-linear evolution towards rupture of the liquid-liquid system is poorly developed as compared to the liquid-solid dewetting. Similarly, stationary droplet solutions for liquid-liquid systems and their stability have been studied numerically by Pototsky et al. [3]. Generalizations to higher dimensions, rigorous proofs are missing and convergence results are still not completely understood. Some of the first results will be given in this work. Moreover, theoretical and experimental investigations suggest that interfacial slip plays a role between liquid layers [8–12]. A systematic derivation of appropriate thin-film models will be given here.

On the experimental side there are some studies on dewetting and film instabilities of liquid-liquid systems [13]. The instability of the liquid-liquid interface are probed either directly in the reciprocal space by neutron reflectometry but without considering the liquid-air interface, or indirectly by the resulting deformation of the liquid-air interface probed by scanning force microscopy [14]. Other groups studied the breakup and the hole growth of a liquid-liquid system, where the viscosity of one of the liquids is much larger than the viscosity of the other liquid [15] and in a very special case, where the resulting dewetting morphologies are all coated with a thin layer of the underlying liquid [16], whereas the characteristic shape of the liquid-liquid interface was not explored in detail. The shape of an underlying liquid polymethylmethacrylate (PMMA) substrate and the liquid polystyrene (PS) rim profile dewetting from this substrate has been studied first in the pioneering work of the group of G. Krausch [17, 18]. As a result, they found a characteristic rim shape and dewetting dynamics, depending on the relative viscosity of the two liquids. The experimentally observed behavior was claimed to be in agreement with Brochard et al. [1] which is surprising since the dewetting velocity strongly depends on film thickness as we will show and which is not considered in [1]. However, the used polymers in [17, 18] are above the entanglement of the respective chain length and viscoelastic properties cannot be ruled out. Here, we explore the dewetting dynamics and undertake a systematic variation of the physical parameters to make quantitative comparisons with our theoretical models. In addition we develop new thin-film models that include nonlinear viscoelastic rheologies.

18.2 Mathematical Model for the Polymer Liquid-Liquid System

We begin this section by introducing the basic setup and notations. Firstly, notice that we consider a two-dimensional situation with the x -axis pointing in horizontal and the z -axis pointing in vertical direction. Later, we give a remark on the generalisation of the models to three dimensions.

We investigate a system of two layered, immiscible fluids on a flat solid substrate which are surrounded by a gas phase (see Fig. 18.1). The lower liquid, which occupies the domain

$$\Omega_1(t) := \{(x, z) \in \mathbb{R}^2; 0 \leq z < h_1(x, t)\}, \tag{18.1}$$

we call liquid 1 or layer 1. Mass density ρ_1 , viscosity μ_1 , pressure p_1 as well as horizontal and vertical velocity components, u_1 and w_1 , are associated with this layer. Similarly, the upper liquid, occupying

$$\Omega_2(t) := \{(x, z) \in \mathbb{R}^2; h_1(x, t) \leq z < h_2(x, t)\}, \tag{18.2}$$

is denoted by liquid 2 or layer 2, with corresponding quantities ρ_2, μ_2, p_2, u_2 and w_2 . For Newtonian liquids the stresses in the n th layer, $n = 1, 2$, are given by

$$\tau_n = -p_n I + \mu_n \begin{pmatrix} 2\partial_x u_n & \partial_z u_n + \partial_x w_n \\ \partial_z u_n + \partial_x w_n & 2\partial_z w_n \end{pmatrix}. \tag{18.3}$$

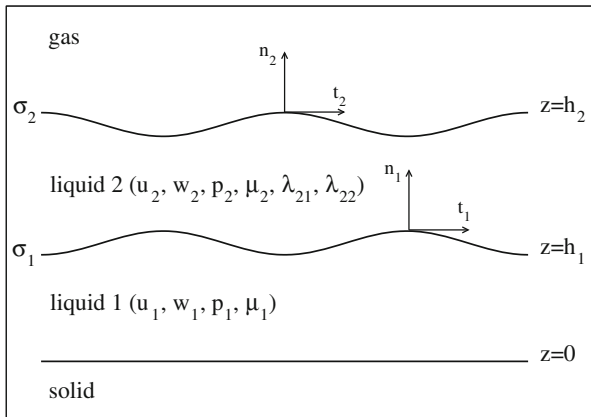


Fig. 18.1 Sketch of a two-layer system

In the case of a viscoelastic upper layer we assume that the symmetric stress tensor τ_2 obeys the corotational Jeffreys model with the constitutive equation

$$\tau_2 + \lambda_{21} \frac{D}{Dt} \tau_2 = \mu_2 \left(\dot{\gamma}_2 + \lambda_{22} \frac{D}{Dt} \dot{\gamma}_2 \right), \quad (18.4)$$

and where the Jaumann derivative D/Dt is defined by

$$\frac{D\Lambda}{Dt} = \frac{d\Lambda}{dt} + \frac{1}{2} (\omega_2 \Lambda - \Lambda \omega_2), \quad (18.5)$$

for an arbitrary tensor field Λ . The strain rate $\dot{\gamma}_2$ is given by

$$\dot{\gamma}_2 = \begin{pmatrix} 2\partial_x u_2 & \partial_z u_2 + \partial_x w_2 \\ \partial_z u_2 + \partial_x w_2 & 2\partial_z w_2 \end{pmatrix}, \quad (18.6)$$

and the vorticity tensor is

$$\omega_2 = \begin{pmatrix} 0 & \partial_x w_2 - \partial_z u_2 \\ \partial_z u_2 - \partial_x w_2 & 0 \end{pmatrix}. \quad (18.7)$$

In this work we assume λ_{21} and λ_{22} to be constant material parameters. The relaxation parameter λ_{21} typically denotes a measure of the time required for the stress to relax to some limiting value, whereas λ_{22} is a measure of the retardation to return to the equilibrium state, see for example [19].

We assume that the system contains three interfaces. The first one between the solid and liquid 1 is located at $z = 0$ and does not change in time t . We call it solid-liquid interface. The tangential and normal vectors of this interface are simply given by $\mathbf{t}_s = (1, 0)$ and $\mathbf{n}_s = (0, 1)$. The other two interfaces evolve in time. The one between the two liquids (liquid-liquid interface) is at $z = h_1(x, t)$ while the free surface between liquid 2 and the gas phase (liquid-gas interface) is at $z = h_2(x, t)$. The unit tangential and normal vectors and the curvatures of the liquid-liquid interface (subindex 1) and the liquid-gas interface (subindex 2) are given by

$$\mathbf{n}_n = \frac{(-\partial_x h_n, 1)}{\sqrt{1 + (\partial_x h_n)^2}}, \quad \mathbf{t}_n = \frac{(1, \partial_x h_n)}{\sqrt{1 + (\partial_x h_n)^2}}, \quad \kappa_n = \frac{\partial_{xx} h_n}{(1 + (\partial_x h_n)^2)^{3/2}}. \quad (18.8)$$

Moreover, we denote the surface tensions for the liquid-liquid and the liquid-gas interface by σ_1 and σ_2 , respectively. For convenience, we also introduce

$$h(x, t) = h_2(x, t) - h_1(x, t), \quad (18.9)$$

the thickness of the top layer as a variable.

Next, we discuss the hydrodynamic equations which describe the evolution of such a system. Then, we introduce a suitable scaling for the variables in this system and obtain a set of nondimensional equations. Finally, using formal asymptotic analysis, we reduce the latter equations to thin film equations for the layer thicknesses, h_1 and h .

18.2.1 Hydrodynamic Equations

In each layer we suppose the Cauchy momentum equations

$$0 = \partial_x u_n + \partial_z w_n, \quad (18.10)$$

$$\rho_n \frac{d}{dt} u_n = -\partial_x p_n + \partial_x \tau_{n,11} + \partial_z \tau_{n,12}, \quad (18.11)$$

$$\rho_n \frac{d}{dt} w_n = -\partial_z p_n + \partial_x \tau_{n,12} + \partial_z \tau_{n,22}, \quad (18.12)$$

where

$$\tau_2 + \lambda_{21} \frac{D}{Dt} \tau_2 = \mu_2 \left(\dot{\gamma}_2 + \lambda_{22} \frac{D}{Dt} \dot{\gamma}_2 \right), \quad (18.13)$$

in the upper layer and

$$\tau_1 = \mu_1 \begin{pmatrix} 2\partial_x u_1 & \partial_z u_1 + \partial_x w_1 \\ \partial_z u_1 + \partial_x w_1 & 2\partial_z w_1 \end{pmatrix}, \quad (18.14)$$

in the lower layer. If $\lambda_{21} = \lambda_{22} = 0$ we are a pure Newtonian case else the upper layer is viscoelastic.

The equations are coupled to each other and to the surrounding solid and gas phase by boundary conditions at the interfaces. At the solid-liquid interface (i.e. $z = 0$), we impose the Navier-slip condition. It says that the tangential component of the velocity is proportional to the shear stress at the interface, or

$$(u_1, w_1) \cdot \mathbf{t}_s = \frac{b}{\mu_1} \mathbf{n}_s \cdot \tau_1 \cdot \mathbf{t}_s. \quad (18.15)$$

The constant b denotes the slip-length. We plug the concrete expressions for \mathbf{t}_s and \mathbf{n}_s into condition (18.15) and obtain

$$u_1 = b \partial_z u_1. \quad (18.16)$$

Besides this we also assume the impermeability condition,

$$w_1 = 0. \quad (18.17)$$

At the liquid-liquid interface, $z = h_1(x, t)$, we have a kinematic condition. It balances the normal component of the velocity of liquid 1 at the interface with the velocity of the interface itself, i.e.

$$(0, \partial_t h_1) \cdot \mathbf{n}_1 = (u_1, w_1) \cdot \mathbf{n}_1. \quad (18.18)$$

Next, we consider capillary forces. These act to reduce the area of the interface and are compensated by the jump of the stress tensors times unit normal vector and also by intermolecular forces, which we explain later,

$$(\tau_1 - \tau_2 - \phi'(h)I) \cdot \mathbf{n}_1 = \sigma_1 \kappa_1 \mathbf{n}_1.$$

Since the last relation is vector valued we obtain two boundary conditions from it,

$$\mathbf{t}_1 \cdot (\tau_1 - \tau_2 - \phi'(h)I) \cdot \mathbf{n}_1 = 0, \quad (18.19)$$

$$\mathbf{n}_1 \cdot (\tau_1 - \tau_2 - \phi'(h)I) \cdot \mathbf{n}_1 = \sigma_1 \kappa_1. \quad (18.20)$$

These are called tangential and normal stress condition, respectively. At this interface we also suppose a slip condition. In contrast to (18.15) the left hand side of the equation depends on the jump of the velocities,

$$(u_2 - u_1, w_2 - w_1) \cdot \mathbf{t}_1 = b_1 \left(\frac{1}{\mu_1} + \frac{1}{\mu_2} \right) \mathbf{n}_1 \cdot \tau_2 \cdot \mathbf{t}_1. \quad (18.21)$$

Notice, the factor $(1/\mu_1 + 1/\mu_2)$ could be chosen in a different way. The advantage of our choice is that slip length b_1 has the unit of a length. Furthermore, in the limit $\mu_1 \rightarrow \infty$, i.e. liquid 1 becomes solid, condition (18.15) is restored. The impermeability condition at this surface reads

$$(u_2 - u_1, w_2 - w_1) \cdot \mathbf{n}_1 = 0. \quad (18.22)$$

The free surface $z = h_2(x, t)$ also evolves according to a kinematic condition,

$$(0, \partial_t h_2) \cdot \mathbf{n}_2 = (u_2, w_2) \cdot \mathbf{n}_2. \quad (18.23)$$

Here, the tangential and normal stress conditions are

$$\mathbf{t}_2 \cdot (\tau_2 + \phi'(h)I) \cdot \mathbf{n}_2 = 0, \quad (18.24)$$

$$\mathbf{n}_2 \cdot (\tau_2 + \phi'(h)I) \cdot \mathbf{n}_2 = \sigma_2 \kappa_2. \quad (18.25)$$

Now let us discuss the intermolecular forces we introduced before (18.19). We investigate a situation in which intermolecular interactions in the layered system give contributions to the surface forces. These additional forces can drive dewetting of the upper liquid. On the other hand, we neglect interactions between liquids 1 and 2 with the solid substrate, which might lead to the breakup of layer 1.

The intermolecular potential for the interactions is given by

$$\phi(h) = \frac{8}{3}\phi_* \left(\frac{1}{8} \left(\frac{h_*}{h} \right)^8 - \frac{1}{2} \left(\frac{h_*}{h} \right)^2 \right). \quad (18.26)$$

This potential consists of two competing terms, which represent long-range, h^{-2} , and short-range, h^{-8} , forces. The long-range term is the disjoining pressure contribution from the van-der-Waals potential. This force drives the dewetting. Only when the thickness h becomes very small the short-range term has an impact. In fact, it stabilises and prevents layer 2 from complete rupture, i.e. no interface between liquid 1 and the gas phase appears. There remains a layer of liquid 2 of very small height. This height is associated with the value h_* for which potential (18.26) has a minimum of $\phi_* < 0$. Notice that while the long-range part in (18.26) can be derived from a Lennard-Jones potential, where also other choices for the form of the stabilising part are possible. A discussion referring to this subject can be found e.g. in Oron et al. [20]. In (18.26) the short-range part of the potential is chosen in order to produce a minimum for a particular thickness of the film. The potential (18.26) gives a contribution to the energy of the system. Variations of h_1 and h_2 change this contribution by $-\phi'(h)\delta h_1$ and $\phi'(h)\delta h_2$, respectively, which produces the extra terms $\phi'(h)$ in (18.20) and (18.25).

The main purpose of the intermolecular potential is to account for the interactions responsible for spinodal dewetting as observed in experiments. This feature will be discussed in the linear stability. With the short-range repulsion term such a potential ensures positivity of solutions, which is a major advantage for the analysis. From a modelling point of view, it also allows to set the equilibrium contact angle and to pass to the Γ -limit of zero precursor thickness, as we will discuss for stationary solutions. However, as this limit is still open for time-dependent solutions, we also discuss algorithms for both situations, i.e. global solutions with precursor and free-boundary problems for the expected sharp-interface model.

18.2.2 Nondimensional Problem

Let H and W be typical scales for the height and the vertical velocity components, respectively. Then, we write

$$z = H\tilde{z}, \quad h_n = H\tilde{h}_n, \quad b = H\tilde{b}, \quad b_1 = H\tilde{b}_1 \quad \text{and} \quad w_n = W\tilde{w}_n. \quad (18.27)$$

Analogously, we denote the characteristic scales for the lateral length and the horizontal velocity by L and U ,

$$x = L\tilde{x}, \quad u_n = U\tilde{u}_n. \quad (18.28)$$

For the characteristic time scale T we suppose $T = L/U$ and set

$$t = \frac{L}{U}\tilde{t}, \quad \lambda_{21} = \frac{L}{U}\tilde{\lambda}_{21}, \quad \lambda_{22} = \frac{L}{U}\tilde{\lambda}_{22}. \quad (18.29)$$

For the stress tensors we set

$$\begin{pmatrix} \tau_{n,11} & \tau_{n,12} \\ \tau_{n,21} & \tau_{n,22} \end{pmatrix} = \frac{\mu_n}{T} \begin{pmatrix} \tau_{n,11}^* & \frac{L}{H}\tau_{n,12}^* \\ \frac{L}{H}\tau_{n,21}^* & \tau_{n,22}^* \end{pmatrix}. \quad (18.30)$$

Furthermore, we assume that the typical scale for the pressure is equal to the one for the intermolecular forces and denote it by P ,

$$p_n = P\tilde{p}_n, \quad \phi' = P\tilde{\phi}'. \quad (18.31)$$

Be aware that in the following we drop ‘ \sim ’. At this point we can choose some of the introduced scales freely. In view of the structure of potential (18.26) we set

$$P = \frac{8}{3} \frac{\phi_*}{H}, \quad (18.32)$$

which results in a rather simple form for ϕ' ,

$$\phi'(h) = \frac{1}{\varepsilon} \left(-\left(\frac{\varepsilon}{h}\right)^9 + \left(\frac{\varepsilon}{h}\right)^3 \right), \quad \text{where } \varepsilon = \frac{h_*}{H}. \quad (18.33)$$

Usually, the minimum point of (18.26), h_* , is much smaller than the characteristic height H . Hence, we suppose $\varepsilon \ll 1$. In the following we use the notations

$$\varepsilon_\ell = \frac{H}{L}, \quad \text{Re} = \frac{\rho_2 U H}{\mu_2}, \quad \rho = \frac{\rho_1}{\rho_2}, \quad \mu = \frac{\mu_1}{\mu_2}, \quad \sigma = \frac{\sigma_1}{\sigma_2}, \quad \alpha = \frac{P H}{\mu_2 U}, \quad (18.34)$$

and we obtain

$$\varepsilon_\ell \rho \text{Re} (\partial_t u_1 + u_1 \partial_x u_1 + w_1 \partial_z u_1) = -\alpha \varepsilon_\ell \partial_x p_1 + \mu (\varepsilon_\ell^2 \partial_{xx} u_1 + \partial_{zz} u_1), \quad (18.35a)$$

$$\varepsilon_\ell^2 \rho \text{Re} (\partial_t w_1 + u_1 \partial_x w_1 + w_1 \partial_z w_1) = -\alpha \partial_z p_1 + \mu (\varepsilon_\ell^3 \partial_{xx} w_1 + \varepsilon_\ell \partial_{zz} w_1), \quad (18.35b)$$

$$0 = \partial_x u_1 + \partial_z w_1, \quad (18.35c)$$

and analogously

$$\varepsilon_\ell \operatorname{Re} (\partial_t u_2 + u_2 \partial_x u_2 + w_2 \partial_z u_2) = -\alpha \varepsilon_\ell \partial_x p_2 + \varepsilon_\ell^2 \partial_x \tau_{2,11} + \partial_z \tau_{2,12}, \quad (18.35d)$$

$$\varepsilon_\ell^2 \operatorname{Re} (\partial_t w_2 + u_2 \partial_x w_2 + w_2 \partial_z w_2) = -\alpha \partial_z p_2 + \varepsilon_\ell \partial_x \tau_{2,21} + \varepsilon_\ell \partial_z \tau_{2,22}, \quad (18.35e)$$

$$0 = \partial_x u_2 + \partial_z w_2, \quad (18.35f)$$

where the stress tensor of the upper liquids fulfil

$$\begin{aligned} & \left(1 + \lambda_{21} \frac{d}{dt}\right) \tau_{2,11} - \lambda_{21} \left(\frac{1}{\varepsilon^2} \partial_z u_2 - \partial_x w_2\right) \tau_{2,12} \\ &= 2 \left(1 + \lambda_{22} \frac{d}{dt}\right) \partial_x u_2 - \lambda_{22} \left(\left(\frac{1}{\varepsilon} \partial_z u_2\right)^2 - (\varepsilon \partial_x w_2)^2\right), \end{aligned} \quad (18.35g)$$

$$\begin{aligned} & \left(1 + \lambda_{21} \frac{d}{dt}\right) \tau_{2,22} + \lambda_{21} \left(\frac{1}{\varepsilon^2} \partial_z u_2 - \partial_x w_2\right) \tau_{2,12} \\ &= 2 \left(1 + \lambda_{22} \frac{d}{dt}\right) \partial_z w_2 + \lambda_{22} \left(\left(\frac{1}{\varepsilon} \partial_z u_2\right)^2 - (\varepsilon \partial_x w_2)^2\right), \end{aligned} \quad (18.35h)$$

$$\begin{aligned} & \left(1 + \lambda_{21} \frac{d}{dt}\right) \tau_{2,12} + \frac{\lambda_{21}}{2} (\partial_z u_2 - \varepsilon^2 \partial_x w_2) (\tau_{2,11} - \tau_{2,22}) \\ &= \left(1 + \lambda_{22} \frac{d}{dt}\right) (\partial_z u_2 + \varepsilon^2 \partial_x w_2) + 2\lambda_{22} (\partial_z u_2 - \varepsilon^2 \partial_x w_2) \partial_x u_2. \end{aligned} \quad (18.35i)$$

The boundary conditions at the substrate, i.e. the impermeability and the Navier-slip condition, now read

$$u_1 = b \partial_z u_1, \quad w_1 = 0. \quad (18.36a)$$

At the liquid-liquid interface, $z = h_1$, we get the following nondimensional equations. For the normal, tangential stresses and the kinematic condition,

$$\begin{aligned} 0 &= p_1 - p_2 + \phi'(h) + 2 \frac{\varepsilon_\ell}{\alpha} \frac{(\mu \partial_z u_1 + \varepsilon_\ell^2 \mu \partial_x w_1 - \tau_{2,12}) \partial_x h_1}{1 + \varepsilon_\ell^2 (\partial_x h_1)^2} + \dots \\ &\quad - \frac{\varepsilon_\ell}{\alpha} \frac{(1 - \varepsilon_\ell^2 (\partial_x h_1)^2) (2\mu \partial_z w_1 - \tau_{2,22})}{1 + \varepsilon_\ell^2 (\partial_x h_1)^2} + \sigma \frac{\partial_{xx} h_1}{(1 + \varepsilon_\ell^2 (\partial_x h_1)^2)^{3/2}}, \end{aligned} \quad (18.36b)$$

$$\begin{aligned} 0 &= (\partial_z u_1 + \varepsilon_\ell^2 \mu \partial_x w_1 - \tau_{2,12}) (1 - \varepsilon_\ell^2 (\partial_x h_1)^2) + \dots \\ &\quad - \varepsilon_\ell^2 (4\mu \partial_x u_1 - 2\tau_{2,11}) \partial_x h_1, \end{aligned} \quad (18.36c)$$

$$\partial_t h_1 = w_1 - u_1 \partial_x h_1. \quad (18.36d)$$

The slip condition becomes

$$(u_2 - u_1) + \varepsilon_\ell^2 (w_2 - w_1) \partial_x h_1 = b_1 \frac{\mu+1}{\mu} \frac{\tau_{2,12}(1-\varepsilon_\ell^2(\partial_x h_1)^2) - 2\varepsilon_\ell^2 \tau_{2,11} \partial_x h_1}{\sqrt{1+\varepsilon_\ell^2(\partial_x h_1)^2}}, \quad (18.36e)$$

and the impermeability condition is given by

$$(w_2 - w_1) - (u_2 - u_1) \partial_x h_1 = 0. \quad (18.36f)$$

Finally, at the liquid-gas interface, $z = h_2$, normal and tangential stresses and the kinematic conditions are

$$0 = p_2 - \phi'(h) - \frac{\varepsilon_\ell}{\alpha} \frac{(1-\varepsilon_\ell^2(\partial_x h_2)^2)\tau_{2,22} - 2\tau_{2,12}\partial_x h_2}{1+\varepsilon_\ell^2(\partial_x h_2)^2} + \frac{\partial_{xx} h_2}{(1+\varepsilon_\ell^2(\partial_x h_2)^2)^{3/2}}, \quad (18.36g)$$

$$0 = \tau_{2,12} \left(1 - \varepsilon_\ell^2 (\partial_x h_2)^2\right) - 2\varepsilon_\ell^2 \tau_{2,11} \partial_x h_2, \quad (18.36h)$$

$$\partial_t h_2 = w_2 - u_2 \partial_x h_2. \quad (18.36i)$$

Note, to write (18.36g) in this form, without loss of generality, we used the balance

$$\frac{\sigma_2 H}{PL^2} = 1 \quad (18.37)$$

This, together with (18.32), determines parameter ε_ℓ ,

$$\varepsilon_\ell = \frac{H}{L} = \sqrt{\frac{8}{3} \frac{\phi_*}{\sigma_2}}. \quad (18.38)$$

To derive thin film equations for the layer thicknesses h_1 and h we assume that $\varepsilon_\ell \ll 1$. In other words, we suppose that the characteristic scale for the height is much smaller than the typical length scale. Equation (18.35a) still depend on several parameters. In the pure Newtonian case we suppose $\lambda_{21} = 0$ and $\lambda_{22} = 0$. While we assume ρ , Re , μ and σ to be of order one w.r.t. ε_ℓ , we consider various magnitudes for the slip lengths b and b_1 . For these different magnitudes, we have to choose alternate α 's and obtain different models. In the viscoelastic case we assume λ_{21} , λ_{22} , ρ , Re and σ to be of order one but μ of order $O(\varepsilon_\ell^2)$. We note that this order of magnitude of μ is the only choice to incorporate the full nonlinear viscoelastic model into an asymptotically consistent thin-film model.

18.3 Thin-Film Model

For no-slip or small interfacial slip we expect that the profile of the lateral velocity component in layer 1 is parabolic. Therefore, we balance the pressure gradient $\partial_x p_1$ with the dominant viscous term $\partial_{zz} u_1$ in (18.35a),

$$\alpha = \frac{1}{\varepsilon_\ell}. \quad (18.39)$$

This fixes the velocity scale and hence, the capillary number,

$$\text{Ca} = \frac{\mu_2 U}{\sigma_2} = \varepsilon_\ell^3. \quad (18.40)$$

After having all the scales fixed we can now derive a thin-film model from (18.35) and (18.36) assuming that $\varepsilon_\ell \ll 1$ and assuming the solutions can be written in asymptotic expansions in ε_ℓ . Using only the leading order terms in the expansions the derivation of thin-film equations from the underlying hydrodynamic model is straight forward, see e.g. [21]. The coupled scaled system of nonlinear fourth order partial differential equations for the profiles of the free surfaces h_1 and h_2 takes the form

$$\partial_t \mathbf{h} = \nabla \cdot (\mathbf{Q} \cdot \nabla \mathbf{p}), \quad (18.41)$$

where $\mathbf{h} = (h_1, h_2)^\top$ is the vector of liquid-liquid interface profile and liquid-air surface profile. The components of the vector $\mathbf{p} = (p_1, p_2)^\top$ are the interfacial pressures given by

$$p_1 = -\sigma \Delta h_1 - \phi'_\epsilon (h_2 - h_1), \quad p_2 = -\Delta h_2 + \phi'_\epsilon (h_2 - h_1), \quad (18.42)$$

The gradient of the pressure vector is multiplied by the mobility matrix \mathbf{Q} which is given by

$$\mathbf{Q} = \frac{1}{\mu} \begin{pmatrix} \frac{h_1^3}{3} & \frac{h_1^3}{3} + \frac{h_1^2(h_2 - h_1)}{2} \\ \frac{h_1^3}{3} + \frac{h_1^2(h_2 - h_1)}{2} & \frac{\mu}{3}(h_2 - h_1)^3 + h_1 h_2 (h_2 - h_1) + \frac{h_1^3}{3} \end{pmatrix}. \quad (18.43)$$

where $\sigma = \sigma_1/\sigma_2$ and $\mu = \mu_1/\mu_2$ denote surface tension and viscosity ratios for the lower and upper layer and $\epsilon = h_*/h_{max}$ is a small parameter with h_{max} being the maximal distance between the polymer-air and polymer-polymer interface.

The energy functional associated to the gradient flow of the lubrication equation can then be given by

$$E_\varepsilon(h_1, h_2) = \int_0^L \left[\frac{\sigma}{2} |\partial_x h_1|^2 + \frac{1}{2} |\partial_x h_2|^2 + \phi_\varepsilon(h_2 - h_1) \right] dx \tag{18.44}$$

where the potential function ϕ_ε denotes the scaled potential with $(n, \ell) = (2, 8)$. The relation to the thin-film equations is $p_i = \delta E_\varepsilon / \delta h_i$.

18.3.1 Mathematical Theory

18.3.1.1 Stationary States

Even though in an actual experiment stationary states represent the late stage of the dewetting process, we begin our analysis with this state, since it allows to identify important quantities, such as the equilibrium Neumann triangle conditions, surface tension and interfacial tensions, by careful comparisons of our mathematical and numerical results with specifically designed experiments. The results of this analysis can then be used in the dynamic models, where other quantities, such as dewetting rates, evolution of interfacial morphologies can be investigated.

We investigated stationary solutions of a thin-film model for liquid two-layer flows with the aim to achieve a rigorous understanding of the contact-angle conditions for such two-layer systems. For this we considered an appropriate energetic formulation that is motivated by its gradient flow structure. We pursued this by investigating a corresponding energy that favors the upper liquid to dewet from the lower liquid substrate, leaving behind a layer of thickness h_* , given by the intermolecular potential

$$\phi(h_2 - h_1) = \frac{\phi_*}{\ell - n} \left[\ell \left(\frac{h_*}{h_2 - h_1} \right)^n - n \left(\frac{h_*}{h_2 - h_1} \right)^\ell \right], \tag{18.45}$$

where h_1 is the height of the liquid-liquid interface, h_2 the height of the free surface and its minimal value $\phi_* < 0$ is attained at h_* . We note that other energies are possible but this one corresponds more closely to the experimental set-up.

One can then obtain that any positive stationary solution of (18.42)–(18.43) satisfies $\partial_x p_1 = \partial_x p_2 = 0$ in Ω . This in turn is equivalent to

$$\sigma \partial_{xx} h_1 = -\phi'_\varepsilon(h_2 - h_1) - \lambda_2 + \lambda_1, \tag{18.46a}$$

$$\partial_{xx} h_2 = \phi'_\varepsilon(h_2 - h_1) - \lambda_1, \tag{18.46b}$$

where constants λ_2 and λ_1 are Lagrange multipliers associated with conservation of mass. We then first established existence of a global minimizer to the energy

functional (18.44) and showed that it satisfies (18.46) with

$$\partial_x h_1 = \partial_x h_2 = \partial_{xxx} h_1 = \partial_{xxx} h_2 = 0 \text{ for } x \in \partial\Omega. \tag{18.47}$$

Theorem 1 *Let Ω be a bounded domain of class $C^{0,1}$ in \mathbb{R}^d , $d \geq 1$ and let $\mathbf{m} = (m_1, m_2)$ with $m_1, m_2 > 0$. Then a global minimizer of $E_\epsilon(\cdot, \cdot)$ defined in (18.44) exists in the class*

$$X_{\mathbf{m}} := \left\{ (h_1, h_2) \in H^1(\Omega)^2 : m_1 = \int_{\Omega} h_1, m_2 = \int_{\Omega} (h_2 - h_1), h_2 \geq h_1 \right\}, \tag{18.48}$$

For $d = 1$ and $\Omega = (0, L)$ the function $h_2 - h_1$ is strictly positive and (h_1, h_2) are smooth solutions to the ODE system (18.46) with (18.47) and

$$\lambda_1 = \frac{1}{L} \int_{\Omega} \phi'_\epsilon(h_2 - h_1) dx, \quad \lambda_2 = 0. \tag{18.49}$$

After proving existence of stationary solutions which is a generalisation of the proof for single-layer thin films [22], we focussed on the limit $h_* \rightarrow 0$ via matched asymptotic analysis in order to recapture the Neumann triangle construction together with the corresponding sharp-interface model. Our analysis shows, that the complete matching of the asymptotic solution requires the inclusion of so-called logarithmic switch-back terms. This is also interesting, in view of the fact that as a limiting case our analysis also includes the case of equilibrium droplets on solid substrates.

We then showed existence and uniqueness of the limit $h_* \rightarrow 0$ within the framework of Γ -convergence and show

Theorem 2 *For the family of energies E_ϵ the Γ -limit is*

$$E_0(h_1, h) = \int_{\Omega} \frac{\sigma}{2} |\nabla h_1|^2 + \frac{1}{2} |\nabla(h_1 + h)|^2 + |\Phi(1)| \chi_{\{h > 0\}}$$

Theorem 3 (Minimizer of Sharp Interface Energy) *Let $\Omega = \mathcal{B}_R(0)$ and $X = \{(h_1, h) \in X_m(\Omega) : h|_{\partial\Omega} = 0\}$ and energy*

$$E(h_1, h) := \int_{\Omega} \frac{\sigma}{2} |\nabla h_1|^2 + \frac{1}{2} |\nabla(h_1 + h)|^2 + |\Phi(1)| \chi_{\{h > 0\}} dx.$$

Then using $\zeta(x) := \alpha(s^2 - |x|^2)^+$ minimizers of E with mass (m_1, m_2) are

$$h_1 = -\frac{1}{\sigma + 1} \zeta(x - x_0) + h_\infty, \quad h(x) = \zeta(x - x_0),$$

with constant $x_0 \in \Omega$ and $s, \alpha, h_\infty \in \mathbb{R}$. Prescribing the mass (m_1, m_2) fixes s and h_∞ , whereas α is fixed by the contact angle (Neumann triangle)

$$\sigma(\nabla h_1)^2 + (\nabla(h_1 + h))^2 = 2|\Phi(1)|, \quad \text{at } |x| = s.$$

Comparison with the sharp-interface model obtained from the Γ -limit agrees with the one obtained via matched asymptotics. Our results on the stationary solutions are published in [23].

18.3.1.2 Existence Theory for the Dynamic Problem

While the existence theory for single layer thin film equations is well established, beginning with the seminal paper by Bernis and Friedman [24], for two-layer systems this seems not to be the case. Only recently, Barrett and El Alaoui [25] introduced a finite element scheme for a similar system including surfactants and investigated existence of weak solutions. However their proof relied on the presence of intermolecular forces in the equations.

In [26] we showed existence of weak solution of the dynamic problem of liquid-liquid thin films and in addition prove non-negativity for the system of degenerate parabolic equations:

$$\begin{aligned} h_{1,t} + (M_{11}p_{1,x} + M_{12}p_{2,x})_x &= 0 \quad \text{in } Q_{T_0} = \Omega \times (0, T_0), \\ h_t + (M_{21}p_{1,x} + M_{22}p_{2,x})_x &= 0 \quad \text{in } Q_{T_0} = \Omega \times (0, T_0), \end{aligned} \tag{18.50}$$

where

$$p_1 = (\sigma + 1)h_{1,xx} + h_{xx}, \quad p_2 = h_{1,xx} + h_{xx}, \quad M = \frac{1}{\mu} \left(\begin{array}{cc} \frac{1}{3}h_1^3 & \frac{1}{2}h_1^2h \\ \frac{1}{2}h_1^2h & \frac{\mu}{3}h^3 + h_1h^2 \end{array} \right). \tag{18.51}$$

For the existence proof for (18.50) we introduce a suitable regularised system.

$$h_{1,t} + ((M_{11} + \delta)p_{1,x} + M_{12}p_{2,x})_x = 0 \quad \text{in } Q_{T_0}, \tag{18.52}$$

$$h_t + (M_{21}p_{1,x} + (M_{22} + \varepsilon)p_{2,x})_x = 0 \quad \text{in } Q_{T_0}, \tag{18.53}$$

where $\delta > 0$ and

$$M = \frac{1}{\mu} \left(\begin{array}{cc} \frac{1}{3}|h_1|^3 & \frac{1}{2}|h_1|^2|h| \\ \frac{1}{2}|h_1|^2|h| & \frac{\mu}{3}|h|^3 + |h_1||h|^2 \end{array} \right) \tag{18.54}$$

This is parabolic in sense of Petrovskiy. Also, initial conditions $h_{1,0}$ and h_0 are approximated in the $H^1(\Omega)$ -norm by $C^{4+\alpha}$ functions $h_{1,0,\delta}$ and $h_{0,\delta}$,

$$h_1(x, 0) = h_{1,0,\delta}(x), \quad h(x, 0) = h_{0,\delta}(x). \tag{18.55}$$

We assume boundary conditions

$$h_{1,x} = h_{1,xxx} = h_x = h_{xxx} = 0 \quad \text{on } x \in \partial\Omega, \tag{18.56}$$

For these conditions using a result by Eidelman [27] shows that (18.52),(18.53), (18.55),(18.56) has a unique solution in a small time interval, say in Q_τ for some $\tau > 0$.

The derivation of uniform upper bounds on the $C_{x,t}^{\frac{1}{2}, \frac{1}{8}}$ -norm of these solutions in Q_τ establishes a priori bounds that allow the conclusion that the solutions can be extended step-by-step to a solution of (18.56), (18.52), (18.53), (18.55) in all of Q_{T_0} . Finally, taking the limit $\varepsilon \rightarrow 0$ existence of weak solutions to (18.50) is established.

Moreover, by exploiting the entropy functional G_δ , which is defined by

$$G_\delta(s) = - \int_s^A g_\delta(r) dr, \quad \text{where} \quad g_\delta(s) = - \int_s^A \frac{dr}{(|r|^n + \delta)^{1/2}}, \quad (18.57)$$

non-negativity of the weak solutions is shown in [26].

18.3.2 Numerical Methods for Liquid-Liquid Dewetting

The goal of this subsection is to discuss different ways of solving the aforementioned free boundary problems numerically. Some care will be taken in emphasizing on how the contact line is dealt with in these approaches. To start with, assume that the dynamics of the two liquids is parameterized by a flow map Ψ_t with $\Omega_i(t) = \Psi(t, \Omega_i(0))$ for $i = 1, 2$. Incompressibility implies that the velocity $\mathbf{u} = \partial_t \Psi$ obeys $\nabla \cdot \mathbf{u} = 0$ in the Eulerian reference frame. For fixed time assume that the domains can be parameterized by functions h_1 and h using

$$\begin{aligned} \Omega_1(t) &:= \{(x, z) \in \mathbb{R} \times \mathbb{R}^+ : 0 < z < h_1(t, x)\}, \\ \Omega_2(t) &:= \{(x, z) \in \mathbb{R} \times \mathbb{R}^+ : h_1(t, x) < z < h_1(t, x) + h(t, x)\}. \end{aligned}$$

Based on this representation of a state of the domains we are going to discuss different strategies to solve the transient problem numerically. Geometrical features can be now discussed in terms of h, h_1 .

18.3.2.1 Stokes Flow with Free Boundaries

For Newtonian viscous liquids $i = 1, 2$ with viscosities μ_i occupying the domains Ω_i it is straightforward to see that the Stokes system admits a variational formulation. Here we restrict to the situation without slip. There one needs to find a (continuous) velocity $\mathbf{u} \in V = H^1(\Omega_1 \cup \Omega_2; \mathbb{R}^2) \cap \{\mathbf{u} : \nabla \cdot \mathbf{u} = 0\}$, such

$$a(\mathbf{u}, \mathbf{v}) = \sum_{i=1}^2 \int_{\Omega_i} \frac{\mu_i}{2} \mathbb{D}(\mathbf{u}) : \mathbb{D}(\mathbf{v}) dx = \sum_{\alpha} \sigma_{\alpha} \int_{\Gamma_{\alpha}} \bar{\nabla} \text{id} : \bar{\nabla} \mathbf{v} ds = f(\mathbf{v}) \quad (18.58)$$

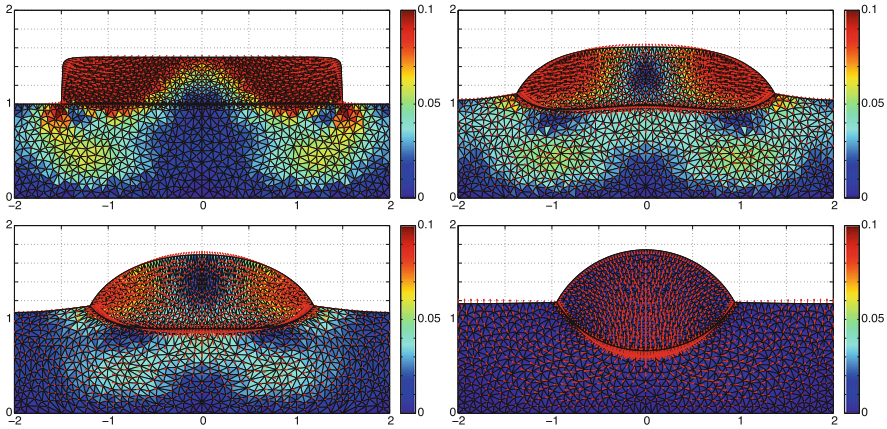


Fig. 18.2 Evolution of a liquid droplet on a liquid substrate into equilibrium $\mu_1 = \mu_2 = \sigma_1 = \sigma_2 = \sigma_3 = 1$. Colors indicate $|\mathbf{u}(x, z)|$, whereas arrows the direction $\mathbf{u}(x, z)/\|\mathbf{u}\|_\infty$

for all $\mathbf{v} \in V$, where σ_α denotes the surface tension of the interface Γ_α . We used the well-known representation of surface tension by the Laplace-Beltrami-operator, which we can write in two dimensions using tangential gradients $\bar{\nabla}$, cf. [28, 29]. Once the velocity is known the domain is moved using the flow map generated by \mathbf{u} . The advantage of (18.58) for the bilayers is that the contact angles (Neumann triangle) can be encoded in energetic structure of the formulation in $f(\mathbf{v})$.

For the numerical discretisation of (18.58) one often employs a finite element (FE) method. Here, one usually transforms the minimization problem into a saddle point problem which, by introducing the pressure as a Lagrange multiplier, enforces the incompressibility $\nabla \cdot \mathbf{u} = 0$. The saddle point problem requires inf-sup stable elements, e.g., Taylor-Hood elements. For this application it makes sense to enrich the pressure space by elements, which allow for a pressure-jump at the liquid-liquid interface. In order to ensure stability of the resulting scheme, one replaces $\text{id} \rightsquigarrow \text{id} + \tau \mathbf{u}$ to create a semi-implicit time-discretisation [28]. After the computation of \mathbf{u} one can move the domain (or all vertices \mathbf{x}_n of the underlying FE mesh) with the Lagrangian velocity field using $\mathbf{x}_n(t + \tau) = \mathbf{x}_n(t) + \tau \mathbf{u}_i$. A snapshot of the solution of the upper layer as it evolves into a stationary liquid lens, is shown in Fig. 18.2. However, the great disadvantage of this approach in our context is the potential inefficiency in situations, where we have a separation of length scales as indicated in the thin-film approximation before.¹ In such a situation the horizontal velocity u_x is basically quadratic in z and the vertical component u_z can be neglected. Then, thin-film models such as (18.41) admit an effective description of the Stokes

¹Typical lengths scales in experiments $[x] = 2 \times 10^4 \text{ nm}$ and $[z] = 10^2 \text{ nm}$.

flow (18.58). The velocity field can be reconstructed from the function h, h_1 and their derivatives with respect to x .

18.3.2.2 Numerical Methods for Thin Film Models

Global Solutions

The corresponding model we need to solve is

$$\partial_t \begin{pmatrix} h \\ h_1 \end{pmatrix} = \nabla \cdot M(h, h_1) \nabla \begin{pmatrix} \pi \\ \pi_1 \end{pmatrix}, \quad (18.59)$$

for $\pi = \delta E / \delta h$ and $\pi_1 = \delta E / \delta h_1$ for some given driving energy $E(h, h_1)$, cf., [30]. Typical energies are of the form

$$E(h, h_1) = \int \frac{\hat{\sigma}}{2} |\nabla(h_1 + h)|^2 + \frac{\hat{\sigma}_1}{2} |\nabla h_1|^2 dx + V(h, h_1). \quad (18.60)$$

The fact how one is going to treat the support of h_1, h and the question, if (18.59) is still a free boundary problem is reflected in the choice of V . For simplicity we are only going to discuss the dependence on h , the discussion for h_1 or composite terms is entirely analogous. When $V \equiv 0$ the liquid spreads over the liquid substrate with zero contact angle. Similarly as in [31–33] one might expect that one can construct algorithms which preserve non-negativity of solutions. These solution might be even smooth enough to be globally (in space) well-defined. Another case, for which we derived a model earlier, is when

$$V(h) = \int \phi_\varepsilon(h) dx \quad (18.61)$$

with ϕ_ε as in (18.26). These models admit a standard variational formulation, for which the semi-implicit time-discretisation is given by

$$\int h^{k+1} v + h_1^{k+1} v_1 + \sum_{ij} \tau M_{ij} \nabla \pi_i \nabla v_j dx = \int h^k v + h_1^k v_1 dx \quad (18.62a)$$

$$\int \pi w + \pi_1 w_1 dx = \int \hat{\sigma} \nabla(h_1 + h) \cdot \nabla(w + w_1) + \hat{\sigma}_2 \nabla h_1 \cdot \nabla w_1 + \phi'_\varepsilon w dx \quad (18.62b)$$

with $h^k(x) = h(\tau k, x)$, $h_1^k(x) = h_1(\tau k, x)$, and M, V are evaluated at $t = \tau k$. The specific choice of ϕ_ε should generally ensure strictly positive solutions which are defined globally in space. However, the kink in the stationary solution for $\varepsilon \rightarrow 0$ already suggests that (local) refinement might be required where the precursor

$h \approx \varepsilon$ meets the support $h \gg \varepsilon$. We solve this problem with standard P1 FEM in one and two space dimensions with natural boundary conditions $\mathbf{n} \cdot \nabla h = 0$ and $\sum_j M_{ij} \mathbf{n} \cdot \nabla \pi_j = 0$.

The Thin-Film Free Boundary Problem

Kriegsmann and Miksis [34] introduced a thin-film model with a sharp triple junction, in which the support of h , i.e., $\omega(t) = \{x : h(t, x) > 0\}$, is part of the unknowns. For quasi-stationary traveling-wave solutions they constructed a scheme to numerically compute h, h_1 . Later, Karapetsas et al. [35] developed a scheme to solve the transient scheme with sharp triple-junctions numerically. However, they needed to use mass conservation as a global property to resolve a numerical singularity near the contact line. Now we are going to explain how this problem can be overcome by systematically using local properties of the variational formulation. Similar to the Stokes equation (18.58) we want to find a variational formulation, which enforces contact angles in a natural way and where the contact line motion is contained in a robust way. For single thin layers such an algorithm has been shown to work in higher dimensions [36] and even for zero contact angle [37].

In contrast to globally defined solutions we have $h : \omega \mapsto \mathbb{R}^+$ and $h_1 : \mathbb{R} \mapsto \mathbb{R}^+$, where we expect kinks in h_1 at triple-junctions $\partial\omega$. First note that the driving functional for this model is

$$V(h) = |\omega| = \int \chi(h) \, dx, \quad \chi(h) = \begin{cases} 1 & h > 0 \\ 0 & \text{else} \end{cases}. \tag{18.63}$$

Since the exact statement of the discrete variational formulation is quite involved, we only state the main differences compared to the standard formulation in (18.62). When we have an evolution of two functions h_1, h encoding domains Ω_1, Ω_2 as explained before, then it is necessary that at the triple junction $(x_c(t), z_c(t))$ we have

$$\lim_{x \searrow x_c} h_1(t, x) = \lim_{x \nearrow x_c} h_1(t, x) = z_c(t), \quad \lim_{x \searrow x_c} h(t, x) = \lim_{x \nearrow x_c} h(t, x) = 0, \tag{18.64}$$

at all times t . This leads to a condition for time-derivatives \dot{h}, \dot{h}_1 of h, h_1

$$\lim_{x \searrow x_c} \dot{h}_1(t, x) + \dot{x}_c \cdot \nabla h_1 = \lim_{x \nearrow x_c} \dot{h}_1(t, x) + \dot{x}_c \cdot \nabla h_1, \tag{18.65}$$

and another condition $\dot{h} + \dot{x}_c \cdot \nabla h = 0$. These are two conditions defining \dot{x}_c and at the same time defining a jump for the time-derivative. This shows that P1 FEM are not suited if we use the Eulerian time-derivatives \dot{h}, \dot{h}_1 as unknowns. We solve this dilemma by allowing the time-derivatives to jump at x_c and enforce the constraints on the jump (18.65) using Lagrange multipliers. As a result this

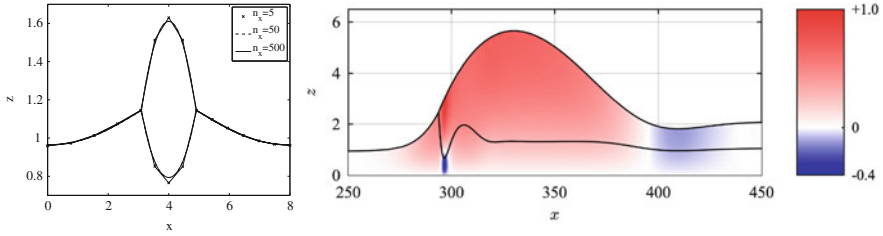


Fig. 18.3 (left) Transient solution of sharp triple-junction problem at various spatial resolutions but same moment in time near a droplet solution and (right) dewetting rim from sharp triple-junction problem with reconstructed velocity fields

condition also delivers the contact line velocity \dot{x}_c without the need to reconstruct it using conservation of mass.

Another non-standard twist is the proper computation of π . Since we define the pressures π as the derivative with respect to h, h_1 , we need to consistently take motion of the domain into account. This is done properly by using Reynolds' transport theorem

$$\frac{d}{dt} \int_{\omega} f(t, x) dx = \int_{\omega} \partial_t f dx + \int_{\partial\omega} f(\dot{x}_c \cdot \mathbf{n}) ds \quad (18.66)$$

$$= \int_{\omega} \partial_t f dx + \int_{\partial\omega} f \frac{\dot{h}}{|\nabla h|} ds, \quad (18.67)$$

where we used $\mathbf{n} = -\nabla h / |\nabla h|$ and $\dot{h} + \dot{x}_c \cdot \nabla h = 0$. By replacing f with the integrand of the energy $E(h, h_1)$ and setting $V(h) = (-\Sigma)|\omega|$ with spreading coefficient Σ this allows the equilibrium contact angle to be included in the variational formulation. Note that the jump condition (18.65) only affects the FE space for \dot{h}, \dot{h}_1 , whereas the FE space for the pressures is continuous. In Fig. 18.3 we show exemplary numerical solutions of such a free boundary problem near a stationary state (left) and during dewetting with reconstructed velocity fields (right).

18.4 Experimental Methods and Comparisons to Theoretical Predictions

For the liquid-liquid dewetting experiments thin polystyrene (PS) films are prepared in their glassy state on top of also glassy thin polymethyl methacrylate (PMMA) films which are supported by silicon wafers. In our various experiments presented here, thicknesses of the underlying PMMA substrate are varied from $h_1 \approx 50$ nm to 700 nm, and the thickness of the dewetting PS film h_2 range from about 5 nm to 250 nm. To prepare those samples, first small rectangular pieces of about 2 cm^2 are

cut from 5''-wafers with (100) orientation. These silicon rectangles are pre-cleaned by a fast CO₂-stream (snow-jet, Tectra) to remove particles. Subsequently, the pre-cleaned silicon wafers are sonicated in ethanol, acetone and toluene, followed by a bath in peroxymonosulfuric acid (piranha etch) to remove organic contaminations. Remains from the peroxymonosulfuric acid are removed by a careful rinse with hot Millipore™ water. After this cleaning procedure PMMA films are spun from toluene solution on top of the silicon support having a homogeneous thicknesses. To achieve the desired film thickness range, toluene solutions with different polymer concentrations (10–100) mg/ml were used. The resulting film thickness is fine tuned by adjusting the rotation speed between 2000 and 6000 rpm using a spin coater from Laurell Technologies (USA). The acceleration of the spin coater was always set at maximum and the spin coating time was about 120 s to make sure that the solvent evaporated during that time. The top PS films can not be spun directly onto the PMMA and are, in a first step, spun from toluene solution onto freshly cleaved mica sheets, following the same protocol as described for the PMMA film. In a second step, the glassy PS films are transferred from mica onto a Millipore™ water surface and picked up from above with the PMMA coated silicon substrates. During the transfer process, the initially closed PS film ruptures into patches which are transferred onto the PMMA substrate.

For our different experiments presented here, PS and PMMA of different molecular chain weights are used, purchased from Polymer Standard Service Mainz (PSS-Mainz, Germany). PS is used with molecular weights of $M_w = 9.6$ kg/mol (PS(9.6k)) and $M_w = 64$ kg/mol (PS(64k)), with polydispersities of $M_w/M_n = 1.03$, and $M_w/M_n = 1.05$, respectively. The used PMMA had a molecular weight of $M_w = 9.9$ kg/mol (PMMA(9.9k)) and a corresponding polydispersities of $M_w/M_n = 1.03$.

The glass transition temperatures of the polymers are $T_{g,PS(9.6k)} = 90 \pm 5$ °C, $T_{g,PS(64k)} = 100 \pm 5$ °C, and $T_{g,PMMA(9.9k)} = 115 \pm 5$ °C. The dewetting experiments are typically conducted at a temperature of $T = 140$ °C resulting in PS viscosities of $\mu_{PS(9.6k)} \approx 2.5$ kPa s and $\mu_{PS(64k)} \approx 700$ kPa s and a PMMA viscosity of $\mu_{PMMA(9.9k)} \approx 675$ kPa s. The viscosity values are measured using the self-similarity in stepped polymer films as presented in [38, 39]. The measured values are in good agreement with viscosities extracted from [40, 41] of $\mu_{PS(9.6k)} \approx 2$ kPa s and $\mu_{PMMA(9.9k)} = 675$ kPa s, respectively. For the numerical calculations of transient droplet profiles we used the viscosities measured by us. The liquid/liquid dewetting process is started by heating the sample above the glass transition temperature and monitored in situ by atomic force microscopy (AFM) at 140 °C in Fastscan Mode™ (Bruker, Germany). To additionally determine the shape of the liquid PS/PMMA interface, the dewetting process is stopped at a desired dewetting stage by quenching the sample from the dewetting temperature $T = 140$ °C down to room temperature. At room temperature both polymers are glassy and the sample can be easily stored and handled. Subsequently the glassy PS structures are removed

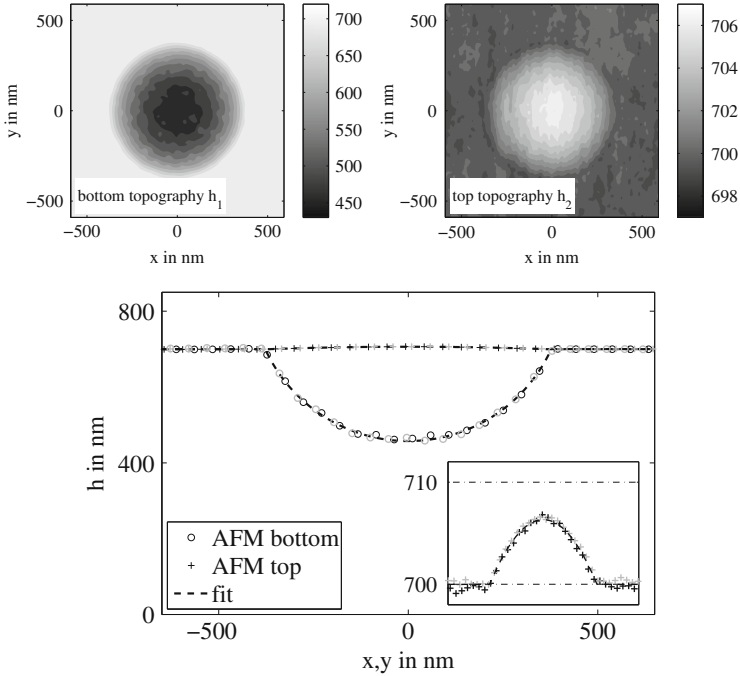


Fig. 18.4 Profile of an equilibrated PS(9.6k) drop swimming on a 700 nm PMMA(9.9k) substrate as determined by AFM. *Top*: The height scales in nanometres are shown to the right of each panel. (*left*) bottom profile h_1 scanned at room temperature and (*right*) top profile h_2 scanned at dewetting temperature. *Bottom*: Two cross sections cut perpendicular through the droplet in x -direction (*dark symbols*) and y -direction (*light symbols*) shown together with the fit using Eq. (18.70) (*dashed line*) in a 1:1 scaling. The inset shows a close up of the top AFM topography with spherical fit. The initially prepared PS and PMMA film thicknesses are 20 and 700 nm, respectively

by a selective solvent (cyclohexane, Sigma Aldrich, Germany) and the formerly PS/PMMA interface is imaged by AFM. The full three dimensional shape of the dewetting PS structures are obtained by combining the subsequently imaged PS/air and PS/PMMA surfaces. The protocol was carefully tested and evaluated to yield accurate results, as described in detail in [42]. To obtain series of such 3D snapshots at different times multiple samples with identical film heights are prepared, each stopped at a different dewetting state and imaged by the above described protocol.

An example for an equilibrium 3d drop shape obtained by the above described protocol is shown in Fig. 18.4. Using the three dimensional PS drop profiles we derived the contact angles and the surface tensions from the equilibrium shapes. These values will serve as input parameters for the simulation of transient droplet morphologies. The corresponding values found in literature [43, 44] are not precise enough and do not provide conclusive predictions on the sign of the spreading coefficient σ . The analysis of the experimental equilibrium drop shapes is given in [42] and leads to the expression for the Neumann-triangle [45], a local condition

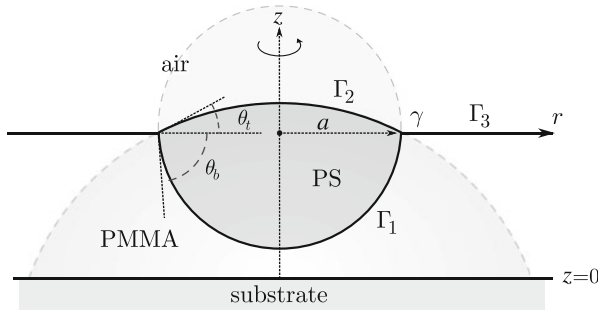


Fig. 18.5 Sketch of an axisymmetric equilibrium droplet

stating that contact angles fulfil the condition

$$\sum_{\alpha=1}^3 \sigma_{\alpha} \mathbf{n}_{\Gamma_{\alpha}} = 0, \tag{18.68}$$

and each interface Γ_{α} has constant mean curvature H_{α} . The normalised vector \mathbf{n}_{α} is tangential to the corresponding interface Γ_{α} and normal to the contact line γ as indicated in Fig. 18.5. For the planar axisymmetric droplets which we observe in the experiments we have $\mathbf{n}_{\Gamma_1} = -\mathbf{e}_r \cos \theta_b - \mathbf{e}_z \sin \theta_b$, $\mathbf{n}_{\Gamma_2} = -\mathbf{e}_r \cos \theta_t + \mathbf{e}_z \sin \theta_t$, $\mathbf{n}_{\Gamma_3} = \mathbf{e}_r$.

One can easily verify that equilibrium droplets as in Eq. (18.68) only exist if the spreading coefficient $\sigma < 0$ and $\sigma_1, \sigma_2 > -\sigma/2$. From a measured equilibrium configuration we can thus extract the values for the surface tensions from Eq. (18.68) using \mathbf{n}_{Γ_i} as follows: If for instance σ_3 is given, then one can determine the other two surface tensions by plugging into solving the linear equation

$$\begin{pmatrix} \cos \theta_t & \cos \theta_b \\ -\sin \theta_t & \sin \theta_b \end{pmatrix} \begin{pmatrix} \sigma_2 \\ \sigma_1 \end{pmatrix} = \begin{pmatrix} \sigma_3 \\ 0 \end{pmatrix}, \tag{18.69}$$

where $\theta_t, \theta_b > 0$ are determined from experimental drop profiles. For contact angles $\theta_t, \theta_b \leq 90^\circ$ a liquid lens has the following axisymmetric equilibrium shape

$$h_2(x, y) = h_{\infty} + \left(\sqrt{H_2^{-2} - r^2} - \sqrt{H_2^{-2} - a^2} \right), \tag{18.70a}$$

$$h_1(x, y) = h_{\infty} - \left(\sqrt{H_1^{-2} - r^2} - \sqrt{H_1^{-2} - a^2} \right), \tag{18.70b}$$

for $r \leq a$ and $h_1(x, y) = h_2(x, y) = h_{\infty}$ for $r > a$. We use the cylindrical coordinates with $r^2 = (x - x_0)^2 + (y - y_0)^2$ and call a the in plane radius of the droplet. A

least-squares fit of (18.70) to the measured AFM profiles shown in Fig. 18.4 return the six parameters h_∞ , H_1 , H_2 , a , x_0 and y_0 .

Since both interfaces, i.e. h_1 and h_2 are measured independently and the AFM can only measure height differences, h_∞ , x_0 , y_0 have no absolute value, so one might define $x_0 = y_0 = 0$ and h_∞ as the values set by the preparation of the PMMA layer and as determined independently. Thus even though a is defined absolutely, due to experimental scatter, one finds slightly varying droplet radii a depending on the analysed AFM profiles h_1 or h_2 but which agree within the experimental resolution of ± 10 nm. Using the values for the constant curvatures H_α and the in-plane radius a the contact angles can be directly computed as r -derivatives of the interfaces h_1 , h_2 in Eq. (18.70) at $r = a$:

$$\theta_b = \arctan \left(a / \sqrt{H_1^{-2} - a^2} \right), \quad (18.71a)$$

$$\theta_t = \arctan \left(a / \sqrt{H_2^{-2} - a^2} \right). \quad (18.71b)$$

Fitting spherical caps (18.70) to the top and bottom profiles of several droplets, see Fig. 18.4, we obtain a relationship between a and H_1 , H_2 , respectively which is shown in Fig. 18.6. For constant contact angles Eq. (18.71) suggest that the relationship between curvature and radius must be linear which is true within the accuracy of the experimental data. From the linear relationship between radius and curvature shown in Fig. 18.6 and using Eq. (18.71) we obtain for the top angle $\theta_t \approx (1.98 \pm 0.07)^\circ$ and for the bottom angle $\theta_b \approx (64 \pm 2)^\circ$ where the error is composed from the statistical error in the fit and the systematic error in

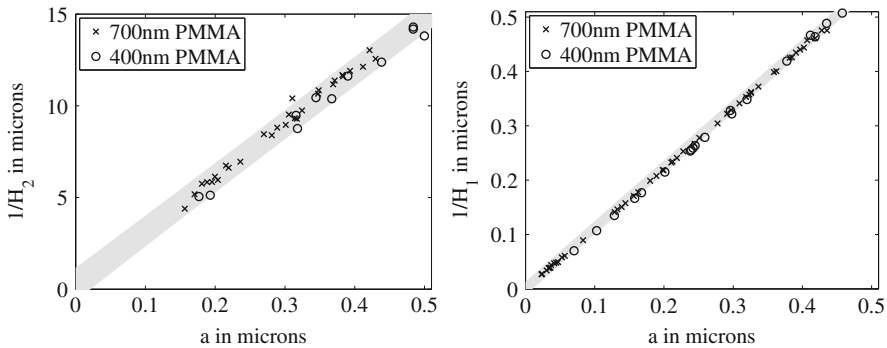


Fig. 18.6 Profiles of PS(9.6k) drops on PMMA(9.9k) substrates. *Top*: Curvature of the top spherical caps and *bottom*: curvature of the bottom spherical caps as a function of droplet radius a measured from equilibrium droplets on 400 nm thick PMMA substrates (*circles*) and 700 nm thick PMMA substrates (*crosses*) with linear fit (*shaded area* 95% confidence interval) gives $H_1^{-1} = (1.11 \pm 0.02)a$ and $H_2^{-1} = (29 \pm 1)a$ and corresponding contact angles $\theta_b = (64 \pm 2)^\circ$ and $\theta_t = (1.98 \pm 0.07)^\circ$

the determination of the droplet radius. Top spherical caps with $a < 150$ nm are not considered in Fig. 18.6 as the height of these drops $\lesssim 2$ nm is comparable to the roughness of the polymer layer. Using Eq. (18.69) we obtain the surface tensions of the PS(9.6k)/PMMA(9.9k) interfaces to

$$\sigma_1 = (0.038 \pm 0.002) \cdot \sigma_3 = (1.22 \pm 0.07) \text{ mN/m},$$

and of the PS/air interface to

$$\sigma_2 = (0.984 \pm 0.001) \cdot \sigma_3 = (31.49 \pm 0.03) \text{ mN/m},$$

based on the PMMA(9.9k)/air surface tension $\sigma_3 = 32$ mN/m at $T = 140$ °C taken from [44]. The corresponding spreading coefficient is

$$\sigma = (-0.022 \pm 0.003)\sigma_3 = (-0.7 \pm 0.1) \text{ mN/m}.$$

The surface tension for the PS(64k)/PMMA(9.9k) combination was determined similarly to $\sigma_\ell = 32.3$ mN/m [46], where the surface tension $\sigma_{\ell,s} = 1.22 \pm 0.07$ mN/m is unchanged. Note that these values and the modification of σ_s are compatible with the literature, e.g. [44].

18.4.1 Nonequilibrium Droplet Shapes

A purely experimental evaluation of the transient droplet shapes using AFM is limited as one can not continuously image the 3d top and bottom shape of a droplet on its journey into equilibrium. In particular the dependence on randomly shaped initial PS patches makes it difficult to describe and understand the morphological evolution on droplets systematically.

To address the question on the dependence of the evolving droplet shapes on the particular choice of the initial configuration theoretically, we choose as initial conditions different cylindrical PS patches of identical volume and fixed thickness of the underlying PMMA film. These patches are then followed numerically towards their respective equilibrium states. A typical example of a time series showing the evolution of the PS droplets with different initial conditions is displayed in Fig. 18.8 for different liquid PS volumes. The chosen initial data correspond to typical droplet volumes observed in our experiments. It is evident from Fig. 18.8 that the characteristic time scale for equilibration strongly depend on the PS volume. For the same dewetting time, a smaller droplet is closer to its equilibrium than a larger one. The results show that for the larger PS volumes (Fig. 18.8) the thicker PS patch quickly develops a characteristic droplet-like shape, with the PS/air interface having almost constant curvature. In contrast, the PS/PMMA interface shows characteristic deformations which are localised around the triple junction and which are evidently different from the equilibrium shape. As discussed before in

dewetting experiments and numerical simulations in [17, 47], surface forces make it energetically favourable to pull the triple junction slightly upward. Note however that this upward-deformation has not been observed for any of the equilibrium states studied in the previous section and is characteristic for the transient nature of the droplet shape. During the further equilibration progress the footprint of the droplet is slightly reduced and the corrugations of the PS/PMMA interface grow in amplitude. The pronounced dents of the PS/PMMA interface finally meet each other forming a dome-like shape of the PS/PMMA interface curved towards the air phase, see $t = 3$ h in the left column and $t = 5$ min in the right column. Remarkably, the curvature of this dome is opposite to the equilibrium drop shape due to the flow squeezing out the PMMA under the droplet. Provided the thickness of the PMMA layer is sufficiently large, the dome-like shape is finally transferred into its equilibrium shape, i.e. a spherical cap curved towards the solid substrate. In case the PMMA film thickness is below this equilibrium penetration depth, the dome-like interface will flatten and touch the solid substrate $h_1 \rightarrow 0$ as $t \rightarrow \infty$, whereas the further equilibration is infinitely slow and self-similar in theory. This self-similar rupture $h_1 \rightarrow 0$ in infinite time has been discussed previously e.g. by Craster and Matar in [47].

When following the transient droplet shapes for the thinner PS patch (dashed lines in the left column of Fig. 18.8) it is evident that the evolution of the drop morphology rather starts from an axisymmetric rim growing inwards the centre of the patch at $r = 0$. The shape of the PS/PMMA interface that forms close to the triple junction is very similar to that for the thicker patch, whereas the PS/air interface develops differently. The initially corners of the PS/air interface are rounded and develop a characteristic profile which are similar to dewetting rim profiles. The initially prepared film thickness remains constant in the centre of the patch until the rim profiles merge and form a drop like profile similar to that of the thick PS patch.

Surprisingly, the transient drop morphologies for a fixed volume and different start configuration synchronise after a certain time and cannot be distinguished any more on their further way into equilibrium. In the examples presented in Fig. 18.8, the synchronisation occurs after about 45 min for the larger PS volume whereas the synchronisation already occurs after about 1 min for the smaller PS volume. For times larger than the synchronisation time the transient droplet morphologies are independent from the specific initial configuration. Moreover, smaller droplets rather have the chance to develop the typical stationary lens shape not touching the underlying substrate. The general behaviour that drops synchronise onto their way towards equilibrium however is not affected by the PS volume.

Finally, the experimentally obtained drop shapes shall be compared to the theoretical predictions. Similar as in the simulations, early stages of droplet-like configurations observed in experiments will depend on the history of the dewetting process and the initial shape of the PS patches and give rise to complex intermediate states, e.g. see Fig. 18.7. Later on, the experimentally observed droplets become axisymmetric with their specific shape independent from that history— at this point the shape is mostly determined by the droplet volume and the total

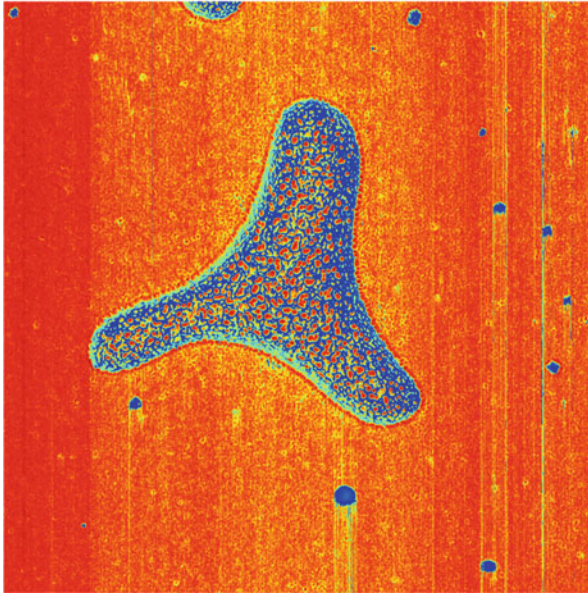


Fig. 18.7 AFM measurement (phase signal) of flower-shaped droplet at early times, where the shape is not yet axisymmetric and depends on the history of the dewetting process

dewetting time. At this point a comparison with simulations makes sense. In the right column of Fig. 18.8 experimentally obtained drop shapes are displayed on top of the theoretical drop shapes for identical volumes after 45 min of dewetting. A visual inspection reveals good agreement of the characteristic morphologies of the transient drop shapes and the time-scales which also emphasises the quality of the (Newtonian) viscosity and the surface tension data. The good agreement between the experimentally determined transient drop shapes and dewetting times indicate moreover that the exact details of the contact angle are not crucial for the drop shape and can be captured precisely by the used thin film model.

18.4.2 Dewetting Rim Profiles

Being able to accurately describe the comparably slow transient drop shapes, we will extend our comparison in the following to the much faster transient rim shapes and their dewetting dynamics. For these experiments the combination of PMMA(9.9k) as liquid substrate and PS(64k) as dewetting liquid is used having about equal viscosities of $\mu \approx 700$ kPa s. The largest Weissenberg number $Wi = \tau\dot{\gamma}$ for the system is calculated, where $\tau = \mu/G$ is the relaxation time with $G = 0.2$ MPa s [48] being the shear modulus of PS. The maximal shear stress for the initial stage of the dewetting is $\dot{\gamma} = 0.05$ s⁻¹ as extracted from the numerical simulations. Taking

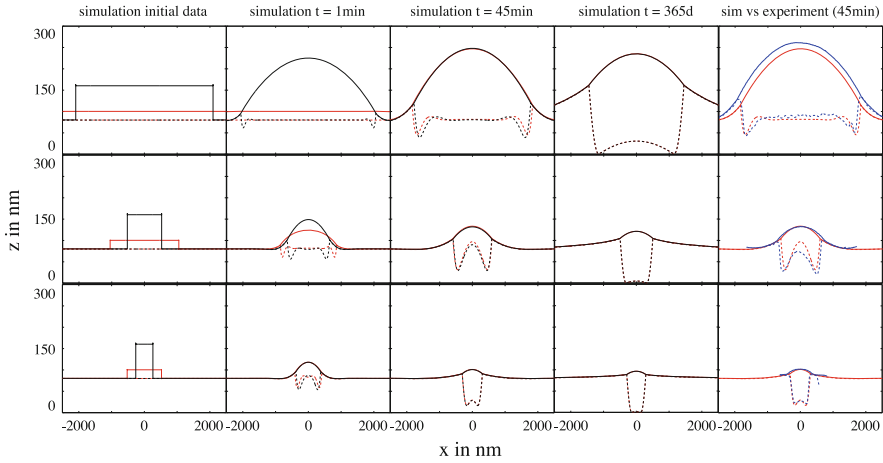


Fig. 18.8 Approach to equilibrium for three different droplet volumes (*top to bottom row*) and two different initial conditions (*red and black*). Initial data in simulations are $h_1(r, 0) = \bar{h}_1$ and $h(r, 0) = \bar{h}$ for $r < r_0$ and $h(r, 0) \approx 0$ (precursor) for $r \geq r_0$ such that the volume $\pi r_0^2 \bar{h}$ matches the experiment. The *right column* compares simulation (*red*) to AFM measurements (*blue*) after 45 min dewetting

all this into account we obtain a Weissenberg number $Wi = 6.25 \times 10^{-3} \ll 1$ and we can safely assume the polymer as purely Newtonian [49].

While most of the experimental parameters are known with an uncertainty fewer than 4%, the viscosity of the used polymers is the main source of uncertainty with the main effect on the timescale of experiment and simulation. Matching experimental and numerical timescales quantitatively by fitting the experimental contact line dynamics, i.e. x_c as a function of time, cf. Fig. 18.9, we obtain a numerical viscosity $\mu_\ell = 1100 \text{ kPa s}$ for both PMMA(9.9k) and PS(64k), which is within experimental accuracy. This viscosity value can be used to quantitatively match experimental and theoretical results for all film thickness ratios and absolute film thicknesses, which are obtained for the same system and at the same temperature. The theoretical prediction that for a fixed film thickness ratio the influence of the absolute height scales linearly is experimentally confirmed by two samples with aspect ratio 1:1 but film thicknesses $\bar{h} \approx 100 \text{ nm}$ and $\bar{h} \approx 240 \text{ nm}$. The dewetting rate appears linear $x_c \sim t$, however, there is no theoretical indication that for aspect ratios and viscosity ratios of order one there should be a power-law dewetting rate. Indeed, further analysis in [46] proves that the velocity slowly decreases over time with transient rates depending on the aspect ratio at hand. This finding confirms previous speculations by Lambooy et al. [50] about the transient nature of the observed dewetting dynamics.

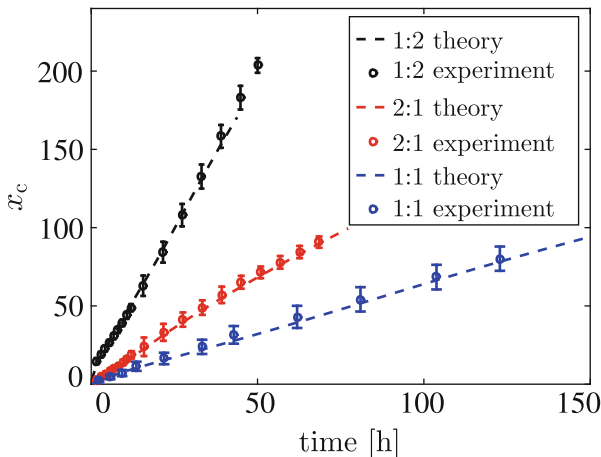


Fig. 18.9 Dewetted distance x_c for aspect ratios 1:1 (240 nm:240 nm), 2:1 (90 nm:45 nm), 1:2 (45 nm:90 nm) from experiment (circles with error) and simulation (dashed lines)

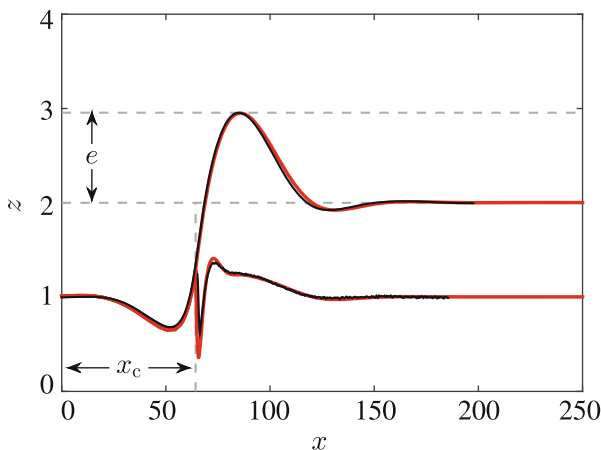


Fig. 18.10 Interfaces from theory (red) and experiment (black) for an aspect ratio of 1:1 and absolute film thicknesses of 240 μm . The experimental cross section is averaged over 30 scan lines of a straight front

In Fig. 18.10 we show the almost perfect alignment of the experimentally measured and theoretically computed interface profiles at identical dewetting times, for equal PMMA and PS film height. The contact line of the dewetting profile is elevated by the flow, a dynamic feature not observed in stationary droplets for sufficiently thick substrates, cf. Figs. 18.4 and 18.6. The material of the dewetting liquid (PS) accumulates in a rim which, by conservation of mass, grows in time when the liquid retracts from the substrate, cf. Fig. 18.10. Also some material of the substrate (PMMA) is dragged along generating a depletion on the “dewetted

side” near the three phase contact line $x < x_c$, and an accumulation of substrate material at the “film side” near the three phase contact line $x > x_c$. Right next to the contact line, some part of the dewetting liquid extends deeply into the substrate and generates a trench and thereby produces additional resistance against the dewetting motion. Note that the size of the trench does not or only weakly depends on the size of the dewetting rim. An equally good agreement between experimental and theoretical rim profiles are obtained also for other film thickness ratios, which can be found in cf. [46]. The only influence of the film thickness ratio on the rim profiles is that for thicker substrates the described features grow, while they shrink for thinner substrates. Away from the rim the interfaces decay in an oscillatory fashion into their prepared constant states $h_1(t, x), h(t, x) \rightarrow \bar{h}_1, \bar{h}$.

We could thus show via quantitative comparisons with experimental results that the thin-film model accurately predicts not only dewetting speeds but also rime shapes of the liquid-liquid dewetting in case of Newtonian liquids and which obey a no-slip boundary condition.

18.5 Role of Interfacial Slip

It has been shown that for polymer films such as PS that dewets from a substrate coated with a hydrophobic molecular monolayer of grafted polymer chains, the dewetting dynamics may exhibit large “apparent” slip [51, 52]. This has been associated with a distinct motion of the polymer chains within a thin region near the boundary of the substrate, as has been argued in Brochard and De Gennes [53], where they showed that for entangled polymer melts an “apparent” slip length b can be related to a microscopic coil-stretch transition into a disentangled state within a thin boundary layer, where the viscosity is much lower. The effect of such an “apparent” slip was investigated in [54, 55], where they showed that slip can control the morphology, dynamics and stability of the system.

For liquid-liquid systems Lin [56] suggested the possibility of interfacial slip. Experimental evidence of slip at polymer-polymer interfaces was given in Zhao and Macosko [10], who investigated PS on PMMA interfaces. A microscopic theory for immiscible blends was developed in Brochard-Wyart and De Gennes [57] and Ajdari [58], and extended by Goveas and Fredrickson [8] and Adhikari and Goveas [9], investigating entangled, unentangled polymer melts as well as polymer emulsions. In particular, expressions for the interfacial viscosity based on the appropriate chain dynamics in this region were derived and the ratio of the bulk and interfacial viscosity was then related to the size of an “apparent” slip length. In summary one can conclude that for two-layer immiscible polymer films the higher shear rate within a thin interfacial region and the associated interfacial viscosity introduces an apparent velocity discontinuity leading to the concept of “apparent” slip.

In the article [59] we have derived thin-film models for the polymer-polymer-solid substrate system and taking account of slip at the solid-polymer as well as the polymer-polymer interfaces. There are a number of cases to consider, such as weak-slip at the polymer-solid interface and weak-slip at the polymer-polymer interface or the case where we assume strong-slip at both interfaces. Then there are also mixed cases and limiting intermediate-slip cases.

18.5.1 The Strong-Slip Case

As we learn from the derivations of single-layer thin film models (see [55]), another distinguished limit for the slip lengths is the order $O(\varepsilon_\ell^{-2})$. Therefore, we consider slip parameters at the solid-liquid and liquid-liquid interface of the form,

$$b = \frac{\beta}{\varepsilon_\ell^2}, \quad b_1 = \frac{\beta_1}{\varepsilon_\ell^2}, \quad (18.72)$$

where β and β_1 are of order $O(1)$. Again, we are motivated by the derivations in [55] and assume plug-flow for the vertical velocity component in layer 1. This leads to

$$\alpha = \varepsilon_\ell. \quad (18.73)$$

Hence, the capillary number is $\text{Ca} = \varepsilon_\ell$. We also introduce the reduced Reynolds number Re^* by

$$\text{Re} = \frac{\rho_2 UH}{\mu_2} = \varepsilon_\ell \frac{\rho_2 \sigma_2 H}{\mu_2^2} = \varepsilon_\ell \text{Re}^*. \quad (18.74)$$

We note that the derivation of the thin-film model for the strong slip case involves also the next-to-leading order in the expansions of the variables in order to obtain a closed model.

18.5.1.1 Leading Order Problem

The leading order bulk equations for layer 1 are given by

$$0 = \partial_{zz}u_1^{(0)}, \quad 0 = -\partial_z p_1^{(0)} + \mu \partial_{zz}w_1^{(0)}, \quad 0 = \partial_x u_1^{(0)} + \partial_z w_1^{(0)}, \quad (18.75)$$

and for layer 2 they read

$$0 = \partial_{zz}u_2^{(0)}, \quad 0 = -\partial_z p_2^{(0)} + \partial_{zz}w_2^{(0)}, \quad 0 = \partial_x u_2^{(0)} + \partial_z w_2^{(0)}. \quad (18.76)$$

For the boundary conditions at the substrate, $z = 0$, we obtain

$$\partial_z u_1^{(0)} = 0, \quad w_1^{(0)} = 0. \quad (18.77)$$

At the liquid-liquid interface $z = h_1^{(0)}$, normal stress, tangential stress and kinematic condition become

$$p_1^{(0)} - p_2^{(0)} + \phi'(h^{(0)}) + \sigma \partial_{xx} h_1^{(0)} - 2 \left((\mu \partial_z w_1^{(0)} - \partial_z w_2^{(0)}) - (\mu \partial_z u_1^{(0)} - \partial_z u_2^{(0)}) \partial_x h_1^{(0)} \right) = 0, \quad (18.78)$$

$$\partial_z (\mu u_1^{(0)} - u_2^{(0)}) = 0, \quad (18.79)$$

$$\partial_t h_1^{(0)} = w_1^{(0)} - u_1^{(0)} \partial_x h_1^{(0)}. \quad (18.80)$$

The slip condition and the impermeability condition at this interface are given by

$$\partial_z u_2^{(0)} = 0, \quad (w_2^{(0)} - w_1^{(0)}) - (u_2^{(0)} - u_1^{(0)}) \partial_x h_1^{(0)} = 0. \quad (18.81)$$

At the free surface $z = h_2^{(0)}$ we get for the normal, tangential and kinematic condition,

$$p_2^{(0)} - \phi'(h^{(0)}) + \partial_{xx} h_2^{(0)} - 2 \left(\partial_z w_2^{(0)} - \partial_z u_2^{(0)} \partial_x h_2^{(0)} \right) = 0, \quad (18.82)$$

$$\partial_z u_2^{(0)} = 0, \quad (18.83)$$

$$\partial_t h_2^{(0)} = w_2^{(0)} - u_2^{(0)} \partial_x h_2^{(0)}. \quad (18.84)$$

We observe that the statement

$$u_1^{(0)} = u_1^{(0)}(x, t), \quad u_2^{(0)} = u_2^{(0)}(x, t), \quad (18.85)$$

results from the first equations in (18.75), (18.76) and boundary conditions (18.77), (18.83). That means that the horizontal velocity components are independent of z . Using this, the continuity equations in (18.75), (18.76) and the impermeability conditions in (18.77), (18.81), we find

$$w_1^{(0)} = -z \partial_x u_1^{(0)}, \quad (18.86)$$

$$w_2^{(0)} = - \left(z - h_1^{(0)} \right) \partial_x u_2^{(0)} - \partial_x u_1^{(0)} h_1^{(0)} + (u_2^{(0)} - u_1^{(0)}) \partial_x h_1^{(0)}. \quad (18.87)$$

Combining the second equations in (18.75) and (18.76) with (18.86) we see that the leading order pressures are also independent of z , i.e.

$$p_2^{(0)} = p_2^{(0)}(x, t), \quad p_1^{(0)} = p_1^{(0)}(x, t). \tag{18.88}$$

Thus we can rewrite the normal stress conditions as

$$p_1^{(0)} = -(\sigma + 1)\partial_{xx}h_1^{(0)} - \partial_{xx}h^{(0)} - 2\mu\partial_xu_1^{(0)}, \tag{18.89}$$

$$p_2^{(0)} = -\partial_{xx}h_1^{(0)} - \partial_{xx}h^{(0)} + \phi'(h^{(0)}) - 2\partial_xu_2^{(0)}. \tag{18.90}$$

To obtain the latter (18.86) is used, too. Next, we derive equations for the thicknesses $h_1^{(0)}$ and $h^{(0)}$ from the leading order kinematic boundary conditions (18.80), (18.84) and formulas (18.86),

$$\partial_t h_1^{(0)} = -\partial_x(u_1^{(0)} h_1^{(0)}), \quad \partial_t h^{(0)} = -\partial_x(u_2^{(0)} h^{(0)}). \tag{18.91}$$

In contrast to the weak-slip case, we cannot deduce closed forms for $u_1^{(0)}$ and $u_2^{(0)}$ from the leading order system. Therefore we have to look at the next order.

18.5.1.2 Next Order Problem

Here, we only state the equations which are necessary in order to fix $u_1^{(0)}$ and $u_2^{(0)}$, and neglect the complete next order problem.

We start with the next order equations in the bulk,

$$\rho\text{Re}^* \left(\partial_t u_1^{(0)} + u_1^{(0)} \partial_x u_1^{(0)} \right) = -\partial_x p_1^{(0)} + \mu \partial_{xx} u_1^{(0)} + \mu \partial_{zz} u_1^{(1)}, \tag{18.92}$$

$$\rho\text{Re}^* \left(\partial_t w_1^{(0)} + u_1^{(0)} \partial_x w_1^{(0)} + w_1^{(0)} \partial_z w_1^{(0)} \right) = -\partial_z p_1^{(1)} + \mu \partial_{xx} w_1^{(0)} + \mu \partial_{zz} w_1^{(1)}, \tag{18.93}$$

$$0 = \partial_x u_1^{(1)} + \partial_z w_1^{(1)}, \tag{18.94}$$

$$\text{Re}^* \left(\partial_t u_2^{(0)} + u_2^{(0)} \partial_x u_2^{(0)} \right) = -\partial_x p_2^{(0)} + \partial_{xx} u_2^{(0)} + \partial_{zz} u_2^{(1)}, \tag{18.95}$$

$$\text{Re}^* \left(\partial_t w_2^{(0)} + u_2^{(0)} \partial_x w_2^{(0)} + w_2^{(0)} \partial_z w_2^{(0)} \right) = -\partial_z p_2^{(1)} + \partial_{xx} w_2^{(0)} + \partial_{zz} w_2^{(1)}, \tag{18.96}$$

$$0 = \partial_x u_2^{(1)} + \partial_z w_2^{(1)}. \tag{18.97}$$

Moreover, we consider the next order of the slip conditions, both at the solid-liquid interface, $z = 0$,

$$u_1^{(0)} = \beta \partial_z u_1^{(1)}, \tag{18.98}$$

and at the liquid-liquid interface, $z = h_1^{(0)}$,

$$u_2^{(0)} - u_1^{(0)} = \beta_1 \frac{\mu + 1}{\mu} \left(\partial_z u_2^{(1)} + \partial_x w_2^{(0)} - 4\partial_x u_2^{(0)} \partial_x h_1^{(0)} \right). \quad (18.99)$$

We also make use of the next order tangential stress boundary conditions at liquid-liquid and the liquid-gas interface,

$$\partial_z \left(\mu u_1^{(1)} - u_2^{(1)} \right) + \partial_x \left(\mu w_1^{(0)} - w_2^{(0)} \right) - 4\partial_x \left(\mu u_1^{(0)} - u_2^{(0)} \right) \partial_x h_1^{(0)} = 0, \quad (18.100)$$

$$\partial_z u_2^{(1)} + \partial_x w_2^{(0)} - 4\partial_x u_2^{(0)} \partial_x h_2^{(0)} = 0. \quad (18.101)$$

Notice, in the equations above we have already used that the z -derivatives of $u_1^{(0)}$ and $u_2^{(0)}$ vanish. When we integrate (18.92) and (18.95) w.r.t. z , we obtain

$$\rho \text{Re}^* h_1^{(0)} \left(\partial_t u_1^{(0)} + u_1^{(0)} \partial_x u_1^{(0)} \right) = h_1^{(0)} \left(-\partial_x p_1^{(0)} + \mu \partial_{xx} u_1^{(0)} \right) + \left(\mu \partial_z u_1^{(1)} \right) \Big|_0^{h_1^{(0)}} \quad (18.102)$$

and, similarly,

$$\text{Re}^* h^{(0)} \left(\partial_t u_2^{(0)} + u_2^{(0)} \partial_x u_2^{(0)} \right) = h^{(0)} \left(-\partial_x p_2^{(0)} + \partial_{xx} u_2^{(0)} \right) + \left(\partial_z u_2^{(1)} \right) \Big|_{h_1^{(0)}}^{h_2^{(0)}}. \quad (18.103)$$

Combining (18.89) and (18.98)–(18.103) leads to

$$\begin{aligned} \rho \text{Re}^* \left(\partial_t u_1^{(0)} + u_1^{(0)} \partial_x u_1^{(0)} \right) &= -\partial_x \left(-(\sigma + 1) \partial_{xx} h_1^{(0)} - \partial_{xx} h^{(0)} \right) \\ &\quad + \frac{4\mu}{h_1^{(0)}} \partial_x (\partial_x u_1^{(0)} h_1^{(0)}) + \frac{\mu(u_2^{(0)} - u_1^{(0)})}{(\mu + 1)\beta_1 h_1^{(0)}} - \frac{\mu u_1^{(0)}}{\beta h_1^{(0)}}, \end{aligned} \quad (18.104)$$

$$\begin{aligned} \text{Re}^* \left(\partial_t u_2^{(0)} + u_2^{(0)} \partial_x u_2^{(0)} \right) &= -\partial_x \left(-\partial_{xx} h_1^{(0)} - \partial_{xx} h^{(0)} + \phi'(h^{(0)}) \right) \\ &\quad + \frac{4}{h^{(0)}} \partial_x (\partial_x u_2^{(0)} h^{(0)}) - \frac{\mu(u_2^{(0)} - u_1^{(0)})}{(\mu + 1)\beta_1 h^{(0)}}. \end{aligned} \quad (18.105)$$

Recalling (18.91), the full model for the leading order velocity fields the leading order layer thicknesses is given by,

$$\begin{aligned} \rho \text{Re}^* \left(\partial_t u_1 + u_1 \partial_x u_1 \right) &= -\partial_x \left(-(\sigma + 1) \partial_{xx} h_1 - \partial_{xx} h \right) \\ &\quad + \frac{4\mu}{h_1} \partial_x (\partial_x u_1 h_1) + \frac{\mu(u_2 - u_1)}{(\mu + 1)\beta_1 h_1} - \frac{\mu u_1}{\beta h_1}, \end{aligned} \quad (18.106)$$

$$\partial_t h_1 = -\partial_x(h_1 u_1), \quad (18.107)$$

$$\begin{aligned} \text{Re}^* (\partial_t u_2 + u_2 \partial_x u_2) &= -\partial_x(-\partial_{xx} h_1 - \partial_{xx} h + \phi'(h)) \\ &\quad + \frac{4}{h} \partial_x(\partial_x u_2 h) - \frac{\mu(u_2 - u_1)}{(\mu + 1)\beta_1 h}, \end{aligned} \quad (18.108)$$

$$\partial_t h = -\partial_x(h u_2), \quad (18.109)$$

where we drop the '(0)'.

In many applications, e.g. dewetting of micro- and nanoscopic polymer films, inertia are negligibly small. Therefore, we assume $\text{Re}^* = 0$ in the following. Then, (18.106) reads

$$\begin{aligned} 0 &= -\partial_x(-(\sigma + 1)\partial_{xx} h_1 - \partial_{xx} h) \\ &\quad + \frac{4\mu}{h_1} \partial_x(\partial_x u_1 h_1) + \frac{\mu(u_2 - u_1)}{(\mu + 1)\beta_1 h_1} - \frac{\mu u_1}{\beta h_1}, \end{aligned} \quad (18.110)$$

$$\partial_t h_1 = -\partial_x(h_1 u_1), \quad (18.111)$$

$$0 = -\partial_x(-\partial_{xx} h_1 - \partial_{xx} h + \phi'(h)) + \frac{4}{h} \partial_x(\partial_x u_2 h) - \frac{\mu(u_2 - u_1)}{(\mu + 1)\beta_1 h}, \quad (18.112)$$

$$\partial_t h = -\partial_x(h u_2). \quad (18.113)$$

We call (18.110) strong-slip model.

18.5.2 The Intermediate-Slip Case

We consider the limits $\beta, \beta_1 \rightarrow 0$ in (18.110) by introducing the scaling

$$u_1 = \beta \tilde{u}_1, \quad u_2 = \beta \tilde{u}_2, \quad t = \frac{\tilde{t}}{\beta}. \quad (18.114)$$

We obtain

$$\begin{aligned} 0 &= -\partial_x(-(\sigma + 1)\partial_{xx} h_1 - \partial_{xx} h) \\ &\quad + \frac{4\mu\beta}{h_1} \partial_x(\partial_x \tilde{u}_1 h_1) + \frac{\mu\beta(\tilde{u}_2 - \tilde{u}_1)}{(\mu + 1)\beta_1 h_1} - \frac{\mu\tilde{u}_1}{h_1}, \end{aligned} \quad (18.115)$$

$$\partial_{\tilde{t}} h_1 = -\partial_x(h_1 \tilde{u}_1), \quad (18.116)$$

$$0 = -\partial_x(-\partial_{xx} h_1 - \partial_{xx} h + \phi'(h)) + \frac{4\beta}{h} \partial_x(\partial_x \tilde{u}_2 h) - \frac{\mu\beta(\tilde{u}_2 - \tilde{u}_1)}{(\mu + 1)\beta_1 h}, \quad (18.117)$$

$$\partial_{\tilde{t}} h = -\partial_x(h \tilde{u}_2). \quad (18.118)$$

Now, let β and β_1 be of order $O(\varepsilon_\ell)$, i.e.

$$\beta = \varepsilon_\ell \tilde{\beta}, \quad \beta_1 = \varepsilon_\ell \tilde{\beta}_1, \quad (18.119)$$

with $\tilde{\beta}$ and $\tilde{\beta}_1$ order one. Then, the leading order in (18.115) is

$$0 = -\partial_x(-(\sigma + 1)\partial_{xx}h_1 - \partial_{xx}h) + \frac{\mu\tilde{\beta}(\tilde{u}_2 - \tilde{u}_1)}{(\mu + 1)\tilde{\beta}_1h_1} - \frac{\mu\tilde{u}_1}{h_1}, \quad (18.120)$$

$$\partial_{\tilde{t}}h_1 = -\partial_x(h_1\tilde{u}_1), \quad (18.121)$$

$$0 = -\partial_x(-\partial_{xx}h_1 - \partial_{xx}h + \phi'(h)) - \frac{\mu\tilde{\beta}(\tilde{u}_2 - \tilde{u}_1)}{(\mu + 1)\tilde{\beta}_1h}, \quad (18.122)$$

$$\partial_{\tilde{t}}h = -\partial_x(h\tilde{u}_2). \quad (18.123)$$

Solving (18.120) and (18.122) for \tilde{u}_1 and \tilde{u}_2 and plugging the result into (18.121) and (18.123), we obtain (dropping ‘ \sim ’):

$$\partial_{\tilde{t}}h_1 = \partial_x(M_{11}\partial_x p_1 + M_{22}\partial_x p_2), \quad (18.124)$$

$$\partial_{\tilde{t}}h = \partial_x(M_{21}\partial_x p_1 + M_{22}\partial_x p_2), \quad (18.125)$$

with the mobility matrix,

$$M = \frac{1}{\mu} \begin{pmatrix} \beta h_1^2 & \beta h_1 h \\ \beta h_1 h & (\beta + (\mu + 1)\beta_1) h^2 \end{pmatrix}, \quad (18.126)$$

and the pressures

$$p_1 = -(\sigma + 1)\partial_{xx}h_1 + \partial_{xx}h, \quad (18.127)$$

$$p_2 = -\partial_{xx}h_1 - \partial_{xx}h + \phi'(h). \quad (18.128)$$

We refer to (18.124) as intermediate-slip model. Notice, rescaling the time by

$$t = \frac{\mu}{\beta} \tilde{t}, \quad (18.129)$$

we can write the mobility matrix M as

$$M = \begin{pmatrix} h_1^2 & h_1 h \\ h_1 h & (1 + \beta_3) h^2 \end{pmatrix}, \quad \text{where } \beta_3 := \frac{(\mu + 1)\beta_1}{\beta}. \quad (18.130)$$

18.5.3 Linear Stability: Influence of Slip

We considered linear stability about the flat states to investigate the spinodal wavelength of the unstable modes.

A rather complex scenario arises, where dispersion curves show transitions from dominant long-wave zig-zag modes to shorter wave varicose modes, depending on the relative thicknesses, viscosities, surface tensions of the layers. What is most interesting is that the presence of interfacial slip can completely change the transitions and the wavelengths of the unstable modes, and hence needs to be accounted for when interpreting experimental results. As an example we show two dispersion relations that demonstrate the impact of slip, from weak to strong, on the spinodal wavelength.

Consider the cases of strong slip at solid/polymer interface, with slip length β_1 and strong slip at polymer-polymer interface, with slip length β_2 . For the new model

$$\begin{aligned} \partial_t h &= -\partial_x [hu_2], & \partial_t h_1 &= -\partial_x (h_1 u_1), \\ 0 &= -\partial_x (\phi'(h) - \partial_{xx} h_1 - \partial_{xx} h) + \frac{4}{h} \partial_x [\partial_x u_2(h)] - \frac{\mu(u_2 - u_1)}{(\mu + 1)\beta_2 h}, \\ 0 &= -\partial_x (-(\sigma + 1)\partial_{xx} h_1 - \partial_{xx} h) + \frac{4\mu}{h_1} \partial_x (\partial_x u_1 h_1) + \frac{\mu(u_2 - u_1)}{(\mu + 1)\beta_2 h_1} - \frac{\mu u_1}{\beta_1 h_1}, \end{aligned}$$

we derived the dispersion relation:

$$\begin{aligned} \omega_{1,2} &= -\frac{k^2}{2} \text{Tr}(\bar{Q} \cdot E) \pm k^2 \sqrt{\frac{\text{Tr}(\bar{Q} \cdot E)^2}{4} - \text{Det}(\bar{Q} \cdot E)}, & \bar{Q} &= -Q_1 T^{-1} Q_2 \\ Q_1 &= \begin{bmatrix} h_1 & 0 \\ 0 & h \end{bmatrix}, & Q_2 &= \begin{bmatrix} \beta_1 \beta h_1 & 0 \\ 0 & \beta h \end{bmatrix}, & E &= \begin{bmatrix} (\sigma + 1)k^2 & k^2 \\ k^2 & k^2 + \phi_h \end{bmatrix} \end{aligned}$$

where $\beta = (1 + \mu)\beta_2$. This we compare to the case for weak slip at both interfaces in Fig. 18.11 below, with dispersion relation

$$\omega_{1,2} = -\frac{k^2}{2} \text{Tr}(\bar{Q} \cdot E) \pm k^2 \sqrt{\frac{\text{Tr}(\bar{Q} \cdot E)^2}{4} - \text{Det}(\bar{Q} \cdot E)}$$

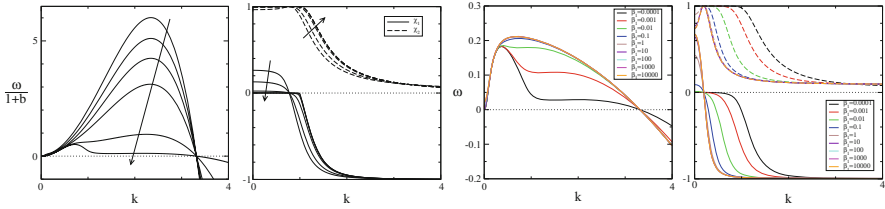


Fig. 18.11 For $h_1 = 10$: Dispersion relations and components of the perturbation vector at both interfaces. For weak-slip with slip length $b = 0, \dots, 10^4$ (left, rescaled by $1 + b$). Arrows point to increasing b . For the strong-slip model for $\beta = 10$, for $\beta_1 = 10^{-4}, \dots, 10^4$ (right)

18.6 The Viscoelastic Case

In this case we consider neither slip nor inertia. Hence, we set $b_1 = b = 0$ as well as $\text{Re} = 0$. Balancing the terms in the stress force conditions yields

$$\frac{\mu_2 U}{\sigma_2} = \varepsilon_\ell, \tag{18.131}$$

and therefore $\alpha = \varepsilon_\ell$. Furthermore we assume

$$\mu := \frac{\mu_1}{\mu_2} \varepsilon^{-2} = O(1), \tag{18.132}$$

keeping the ratio of the surface tensions $\sigma := \sigma_1/\sigma_2 = O(1)$.

We will now show that to leading order in ε the free boundary problem can be integrated and reduced to a system of coupled partial differential equations for the height h, h_1, u_2 and S . To leading order the equations in the bulk of the lower liquid and in the upper liquid are

$$\partial_x u_1 + \partial_z w_1 = 0, \quad 0 = -\partial_x p_1 + \mu \partial_{zz} u_1, \quad 0 = -\partial_z p_1 \tag{18.133}$$

and

$$\partial_x u_2 + \partial_z w_2 = 0, \quad 0 = \partial_z \tau_{2,12}, \quad 0 = -\partial_z p_2 + \partial_x \tau_{2,12} + \partial_z \tau_{2,22}, \tag{18.134}$$

where

$$\lambda_{21} \partial_z u_2 \tau_{2,12} = \lambda_{22} (\partial_z u_2)^2 \tag{18.135}$$

and

$$\left(1 + \lambda_{21} \frac{d}{dt}\right) \tau_{2,12} + \frac{\lambda_{21}}{2} \partial_z u_2 (\tau_{2,11} - \tau_{2,22}) = \left(1 + \lambda_{22} \frac{d}{dt}\right) \partial_z u_2 + 2\lambda_{22} \partial_z u_2 \partial_x u_2. \quad (18.136)$$

The boundary conditions are

$$u_1 = 0, \quad w_1 = 0 \quad (18.137)$$

at $z = 0$,

$$\partial_t h_1 = w_1 - \partial_x h_1 u_1, \quad (18.138)$$

$$\tau_{2,12} = 0, \quad -p_1 + p_2 - \phi'(h) - \tau_{2,22} = \sigma \partial_{xx} h_1, \quad (18.139)$$

$$u_2 - u_1 = 0, \quad -(u_2 - u_1) \partial_x h_1 + (w_2 - w_1) = 0, \quad (18.140)$$

at $z = h_1$ and

$$\partial_t h_2 = w_2 - \partial_x h_2 u_2, \quad (18.141)$$

$$\tau_{2,12} = 0, \quad -p_2 + \phi'(h) + \tau_{2,22} = \partial_{xx} h_2 \quad (18.142)$$

at $z = h_2$.

In order to obtain a closed set of equation we also need to account for the relations for the stress tensor from the next order problem, where we have expanded the variables $u_i, w_i, p_i, \tau_{i,jk}$ with $i, j, k \in 1, 2$ as $u_i = u_i^{(0)} + \varepsilon^2 u_i^{(1)} + O(\varepsilon^4)$ and likewise with the other variables. For ease of notation we then dropped the index ⁽⁰⁾ from the leading order variables. The relations we need are,

$$0 = -\partial_x p_2 + \partial_x \tau_{2,11} + \partial_z \tau_{2,12}^{(1)}, \quad (18.143)$$

$$\left(1 + \lambda_{21} \frac{d}{dt}\right) \tau_{2,11} = 2 \left(1 + \lambda_{22} \frac{d}{dt}\right) \partial_x u_2, \quad (18.144)$$

$$\left(1 + \lambda_{21} \frac{d}{dt}\right) \tau_{2,22} = 2 \left(1 + \lambda_{22} \frac{d}{dt}\right) \partial_z w_2, \quad (18.145)$$

which hold for $(x, z, t) \in \Omega_2$ as well as

$$(\mu \partial_z u_1 - \tau_{2,12}^{(1)}) - (\tau_{2,22} - \tau_{2,11}) \partial_x h_1 = 0, \quad (18.146)$$

at $z = h_1$ and

$$\tau_{2,12}^{(1)} + (\tau_{2,22} - \tau_{2,11}) \partial_x h_2 = 0, \quad (18.147)$$

at $z = h_2$.

Our first observation is that integrating the leading order momentum balance equations for the upper layer (18.134) w.r.t. z and using the boundary condition (18.142) gives

$$p_2 = \tau_{2,22} - \partial_{xx} h_1 - \partial_{xx} h + \phi'(h). \quad (18.148)$$

Combining this expression with the next order momentum balance (18.143) we obtain

$$0 = \partial_x(\partial_{xx} h_1 + \partial_{xx} h - \phi'(h)) + \partial_x(\tau_{2,11} - \tau_{2,22}) + \partial_z \tau_{2,12}^{(1)}. \quad (18.149)$$

We set

$$\bar{\tau}_2 := \tau_{2,11} - \tau_{2,22}. \quad (18.150)$$

Then integration of Eq. (18.149) gives

$$0 = h \partial_x(\partial_{xx} h_1 + \partial_{xx} h - \phi'(h)) + \int_{h_1}^{h_2} \partial_x \bar{\tau}_2 dz + \tau_{2,12}^{(1)}|_{z=h_2} - \tau_{2,12}^{(1)}|_{z=h_1}. \quad (18.151)$$

If we use this expression together with the next order boundary conditions (18.146)–(18.147) and set

$$S := \frac{1}{4h} \int_{h_1}^{h_2} \bar{\tau}_2 dz, \quad (18.152)$$

we obtain

$$0 = h \partial_x(\partial_{xx} h_1 + \partial_{xx} h - \phi'(h)) + 4 \partial_x(hS) - \mu \partial_z u_1|_{z=h_1}. \quad (18.153)$$

In the next step we derive an equation for S . We first note that because of (18.134)–(18.135) and (18.139) $u_2 = u_2(x, t)$ does not depend on z . We combine (18.144) and (18.145) to

$$\left(1 + \lambda_{21} \frac{d}{dt}\right) \bar{\tau}_2 = 4(1 + \lambda_{22} \partial_t + \lambda_{22} u_2 \partial_x) \partial_x u_2. \quad (18.154)$$

Integration of the left hand side of this equation yields

$$\int_{h_1}^{h_2} \left(1 + \lambda_{21} \frac{d}{dt}\right) \bar{v}_2 dz \quad (18.155)$$

$$= \int_{h_1}^{h_2} (1 + \lambda_{21} \partial_t + \lambda_{21} u_2 \partial_x + \lambda_{21} w_2 \partial_z) \bar{v}_2 dz \quad (18.156)$$

$$= \int_{h_1}^{h_2} (1 + \lambda_{21} \partial_t + \lambda_{21} u_2 \partial_x + \lambda_{21} (-z \partial_x u_2 + \partial_t h_1 + \partial_x (u_2 h_1))) \bar{v}_2 dz \quad (18.157)$$

$$= 4h(1 + \lambda_{21} \partial_t + \lambda_{21} u_2 \partial_x) S \quad (18.158)$$

Hence, we obtain the equation for S

$$(1 + \lambda_{21} \partial_t + \lambda_{21} u_2 \partial_x) S = (1 + \lambda_{22} \partial_t + \lambda_{22} u_2 \partial_x) \partial_x u_2. \quad (18.159)$$

The kinematic and impermeability conditions imply the equation for h

$$\partial_t h = -\partial_x (h u_2). \quad (18.160)$$

In the last step we consider the evolution of the lower fluid and the interface h_1 . From (18.133) and (18.137) we first obtain

$$u_1 = \frac{1}{2\mu} \partial_x p_1 z^2 + c z, \quad (18.161)$$

which we use for the evolution equation for h_1

$$\partial_t h_1 = -\partial_x \int_0^{h_1} u_1 dz = -\partial_x \left(\frac{1}{6\mu} h_1^3 \partial_x p_1 + \frac{1}{2} h_1^2 c \right). \quad (18.162)$$

and determine the constant c from equation

$$\frac{1}{2\mu} \partial_x p_1 h_1^2 + c h_1 = u_2 \quad (18.163)$$

and by using (18.140). We finally obtain the closed system of equations for h_1 , h , S and u_2 .

$$\partial_t h = -\partial_x (h u_2), \quad (18.164)$$

$$\partial_t h_1 = \frac{1}{12\mu} \partial_x (h_1^3 \partial_x p_1) - \frac{1}{2} \partial_x (h_1 u_2), \quad (18.165)$$

$$0 = -\frac{1}{2} h_1 \partial_x p_1 - h \partial_x p_2 + 4 \partial_x (h S) - \frac{\mu}{h_1} u_2, \quad (18.166)$$

$$0 = (1 + \lambda_{21} \partial_t + \lambda_{21} u_2 \partial_x) S - (1 + \lambda_{22} \partial_t + \lambda_{22} u_2 \partial_x) \partial_x u_2. \quad (18.167)$$

where

$$p_1 = -(\sigma + 1)\partial_{xx}h_1 - \partial_{xx}h, \quad \text{and} \quad p_2 = -\partial_{xx}h_1 - \partial_{xx}h + \phi'(h). \quad (18.168)$$

The above model is the first model that incorporates the full nonlinear corotational Jeffrey's model into a thin-film theory. Using this model it is now possible to analyse and numerically investigate the nonlinear behaviour and long-time morphological evolution of dewetting liquid-liquid films. This will be subject of future work.

18.7 Conclusion

In this chapter, we considered the liquid-liquid dewetting, where a thin liquid film retracts from an also thin liquid substrate. Mathematical models based on the thin film equation are derived including models that take account of interfacial apparent slip and nonlinear viscoelastic effects. For the Newtonian case, existence results for the stationary and dynamic problems as well as numerical methods for the thin-film as well as the underlying free boundary problem for the Stokes equations were presented.

For the case of Newtonian liquids the theoretical predictions were quantitatively compared to experimental results obtained by polystyrene (PS) dewetting from polymethyl-methacrylate (PMMA). Both polymers were used with sufficiently short molecular chain length and could be considered as Newtonian liquids. The relevant system parameters like viscosity, contact angle and surface tension were determined for the experimental system and used as input parameters for the mathematical model. The quantitative comparison proved that thin-film models are adequate to describe transient dewetting rim and droplet shapes as well as dewetting dynamics which result from a complex interaction of substrate and liquid flow.

Another important problem that is currently being investigated concerns the spinodal dewetting process, investigating the self-similar evolution towards rupture. An interesting question is if this occurs in finite time. In the future we also will carry out comparisons of solutions of our viscoelastic thin-film model with experimental results by repeating our experiments for different chain length of both polymers to vary the rheological properties.

References

1. Brochard Wyart, F., Martin, P., Redon, C.: Liquid/liquid dewetting. *Langmuir* **9**(12), 3682–3690 (1993)
2. Pototsky, A., Bestehorn, M., Merkt, D., Thiele, U.: Alternative pathways of dewetting for a thin liquid two-layer film. *Phys. Rev. E* **70**(2), 25201 (2004)

3. Pototsky, A., Bestehorn, M., Merkt, D., Thiele, U.: Morphology changes in the evolution of liquid two-layer films. *J. Chem. Phys.* **122**, 224711 (2005)
4. Fisher, L.S., Golovin, A.A.: Nonlinear stability analysis of a two-layer thin liquid film: Dewetting and autophobic behavior. *J. Colloid Interface Sci.* **291**(2), 515–528 (2005)
5. Fisher, L.S., Golovin, A.A.: Instability of a two-layer thin liquid film with surfactants: dewetting waves. *J. Colloid Interface Sci.* **307**(1), 203–214 (2007)
6. Bandyopadhyay, D., Gulabani, R., Sharma, A.: Instability and dynamics of thin liquid bilayers. *Ind. Eng. Chem. Res.* **44**(5), 1259–1272 (2005)
7. Bandyopadhyay, D., Sharma, A.: Nonlinear instabilities and pathways of rupture in thin liquid bilayers. *J. Chem. Phys.* **125**, 054711 (2006)
8. Goveas, J.L., Fredrickson, G.H.: Apparent slip at a polymer-polymer interface. *Eur. Phys. J. B* **2**(1), 79–92 (1998)
9. Adhikari, N.P., Goveas, J.L.: Effects of slip on the viscosity of polymer melts. *J. Polym. Sci. B Polym. Phys.* **42**, 1888–1904 (2004)
10. Zhao, R., Macosko, C.W.: Slip at polymer-polymer interfaces: Rheological measurements on coextruded multilayers. *J. Rheol.* **46**, 145–167 (2002)
11. Lin, Z., Kerle, T., Russell, T.P., Schaffer, E., Steiner, U.: Electric field induced dewetting at polymer/polymer interfaces. *Macromolecules* **35**(16), 6255–6262 (2002)
12. Zeng, H., Tian, Y., Zhao, B., Tirrell, M., Israelachvili, J.: Friction at the liquid/liquid interface of two immiscible polymer films. *Langmuir* **25**, 124–132 (2009)
13. Higgins, A.M., Sferrazza, M., Jones, R.A.L., Jukes, P.C., Sharp, J.S., Dryden, L.E., Webster, J.: The timescale of spinodal dewetting at a polymer/polymer interface. *Eur. Phys. J. E* **8**, 137–143 (2002)
14. de Silva, J.P., Geoghegan, M., Higgins, A.M., Krausch, G., David, M.O., Reiter, G.: Switching layer stability in a polymer bilayer by thickness variation. *Phys. Rev. Lett.* **98**(26), 267802 (2007)
15. Segalman, R.A., Green, P.F.: Dynamics of rims and the onset of spinodal dewetting at liquid/liquid interfaces. *Macromolecules* **32**(3), 801–807 (1999)
16. Slep, D., Asselta, J., Rafailovich, M.H., Sokolov, J., Winesett, D.A., Smith, A.P., Ade, H., Anders, S.: Effect of an interactive surface on the equilibrium contact angles in bilayer polymer films. *Langmuir* **16**, 2369–2375 (2000)
17. Lambooy, P., Phelan, K.C., Haugg, O., Krausch, G.: Dewetting at the liquid-liquid interface. *Phys. Rev. Lett.* **76**(7), 1110–1113 (1996)
18. Wang, C., Krausch, G., Geoghegan, M.: Dewetting at a polymer-polymer interface: film thickness dependence. *Langmuir* **17**(20), 6269–6274 (2001)
19. Hassager, O., Bird, R.B., Armstrong, R.C.: *Dynamics of Polymeric Fluids*, vol. 1. Wiley, New York (1977)
20. Oron, A., Davis, S.H., Bankoff, S.G.: Long-scale evolution of thin liquid films. *Rev. Mod. Phys.* **69**(3), 931 (1997)
21. Kostourou, K., Peschka, D., Münch, A., Wagner, B., Herminghaus, S., Seemann, R.: Interface morphologies in liquid/liquid dewetting. *Chem. Eng. Process.* **50**, 531–536 (2011)
22. Bertozzi, A.L., Grün, G., Witelski, T.P.: Dewetting films: bifurcations and concentrations. *Nonlinearity* **14**, 1569 (2001)
23. Jachalski, S., Huth, R., Kitavtsev, G., Peschka, D., Wagner, B.: Stationary solutions for two-layer lubrication equations. *SIAM J. Appl. Math.* **73**(3), 1183–1202 (2013)
24. Bernis, F., Friedman, A.: Higher order nonlinear degenerate parabolic equations. *J. Differ. Equ.* **83**(1), 179–206 (1990)
25. Barrett, J.W., El Alaoui, L.: Finite element approximation of a two-layered liquid film in the presence of insoluble surfactants. *ESAIM: Math. Model. Numer. Anal.* **42**(05), 749–775 (2008)
26. Jachalski, S., Kitavtsev, G., Taranets, R.: Weak solutions to lubrication system describing the evolution of bilayer thin films. *Commun. Math. Sci.* **30**(3), 527–544 (2014)
27. Eidel'man, S.D.: *Parabolic Systems*. North Holland, Amsterdam (1969)
28. Bänsch, E.: Finite element discretization of the Navier–Stokes equations with a free capillary surface. *Numer. Math.* **88**(2), 203–235 (2001)

29. Dziuk, G.: Finite elements for the Beltrami operator on arbitrary surfaces. In: *Partial Differential Equations and Calculus of Variations*, pp. 142–155. Springer, Berlin (1988)
30. Huth, R., Jachalski, S., Kitavtsev, G., Peschka, D.: Gradient flow perspective on thin-film bilayer flows. *J. Eng. Math.* **94**(1), 43–61 (2015)
31. Zhornitskaya, L., Bertozzi, A.L.: Positivity-preserving numerical schemes for lubrication-type equations. *SIAM J. Numer. Anal.* **37**(2), 523–555 (1999)
32. Grün, G., Rumpf, M.: Nonnegativity preserving convergent schemes for the thin film equation. *Numer. Math.* **87**(1), 113–152 (2000)
33. Diez, J.A., Kondic, L.: Computing three-dimensional thin film flows including contact lines. *J. Comput. Phys.* **183**(1), 274–306 (2002)
34. Kriegsmann, J.J., Miksis, M.J.: Steady motion of a drop along a liquid interface. *SIAM J. Appl. Math.* **64**(1), 18–40 (2003)
35. Karapetsas, G., Craster, R.V., Matar, O.K.: Surfactant-driven dynamics of liquid lenses. *Phys. Fluids* **23**(12), 122106–122106 (2011)
36. Peschka, D.: Thin-film free boundary problems for partial wetting. *J. Comput. Phys.* **295**, 770–778 (2015)
37. Peschka, D.: Numerics of contact line motion for thin films. *IFAC-PapersOnLine* **48**(1), 390–393 (2015)
38. McGraw, J.D., Salez, T., Bäümchen, O., Raphaël, E., Dalnoki-Veress, K.: Self-similarity and energy dissipation in stepped polymer films. *Phys. Rev. Lett.* **109**, 128303 (2012)
39. Salez, T., McGraw, J.D., Cormier, S.L., Bäümchen, O., Dalnoki-Veress, K., Raphaël, E.: Numerical solutions of thin-film equations for polymer flows. *Eur. Phys. J. E* **35**(11), 1–9 (2012)
40. Herminghaus, S., Jacobs, K., Seemann, R.: The glass transition of thin polymer films: some questions, and a possible answer. *Eur. Phys. J. E* **5**(5), 531–538 (2001)
41. Bäümchen, O., Fetzer, R., Klos, M., Lessel, M., Marquant, L., Häh, H., Jacobs, K.: Slippage and nanorheology of thin liquid polymer films. *J. Phys. Condens. Matter* **24**(32), 325102 (2012)
42. Bommer, S., Cartellier, F., Jachalski, S., Peschka, D., Seemann, R., Wagner, B.: Droplets on liquids and their journey into equilibrium. *Eur. Phys. J. E* **36**(8), 1–10 (2013)
43. Anastasiadis, S.H., Gancarz, I., Koberstein, J.T.: Interfacial tension of immiscible polymer blends: temperature and molecular weight dependence. *Macromolecules* **21**(10), 2980–2987 (1988)
44. Wu, S.: Surface and interfacial tensions of polymer melts. II. Poly (methyl methacrylate), poly (n-butyl methacrylate), and polystyrene. *J. Phys. Chem.* **74**(3), 632–638 (1970)
45. Neumann, F.E.: *Vorlesung über die Theorie der Capillarität*. BG Teubner, Leipzig (1894)
46. Bommer, S., Jachalski, S., Peschka, D., Seemann, R., Wagner, B.: Rates and morphology in liquid-liquid dewetting. *WIAS Preprint* 2346 (2016)
47. Craster, R.V., Matar, O.K.: On the dynamics of liquid lenses. *J. Colloid Interface Sci.* **303**(2), 503–516 (2006)
48. Rubenstein, M., Colby, R.H.: *Polymer Physics*. Oxford University Press, Oxford (2003)
49. Morozov, A.N., van Saarloos, W.: An introductory essay on subcritical instabilities and the transition to turbulence in visco-elastic parallel shear flows. *Phys. Rep.* **447**(3), 112–143 (2007)
50. Lambooy, P., Phelan, K.C., Haugg, O., Krausch, G.: Dewetting at the liquid-liquid interface. *Phys. Rev. Lett.* **76**(7), 1110 (1996)
51. Fetzer, R., Jacobs, K., Münch, A., Wagner, B., Witelski, T.P.: New slip regimes and the shape of dewetting thin liquid films. *Phys. Rev. Lett.* **95**, 127801 (2005)
52. Redon, C., Brzoska, J.B., Brochard-Wyart, F.: Dewetting and slippage of microscopic polymer films. *Macromolecules* **27**(2), 468–471 (1994)
53. Brochard-Wyart, F., de Gennes, P.G.: Shear-dependent slippage at a polymer/solid interface. *Langmuir* **8**, 3033–3037 (1992)
54. Kargupta, K., Sharma, A., Khanna, R.: Instability, dynamics and morphology of thin slipping films. *Langmuir* **20**, 244–253 (2004)
55. Münch, A., Wagner, B., Witelski, T.P.: Lubrication models with small to large slip lengths. *J. Eng. Math.* **53**, 359–383 (2006)

56. Lin, C.C.: A mathematical model for viscosity in capillary extrusion of two-component polyblends. *Polym. J. (Tokyo)* **11**, 185–192 (1979)
57. Brochard-Wyart, F., de Gennes, P.-G.: Sliding molecules at a polymer/polymer interface. *C.R. Acad. Sci., Ser. II* **317**, 13–17 (1993)
58. Ajdari, A.: Slippage at a polymer/polymer interface: entanglements and associated friction. *C.R. Acad. Sci., Ser. II* **317**, 1159–1163 (1993)
59. Jachalski, S., Münch, A., Peschka, D., Wagner, B.: Impact of interfacial slip on the stability of liquid two-layer films. *J. Eng. Math.* **86**, 9–29 (2014)